Support effect on Ni-based catalysts using methane decomposition

analysed from

in-situ TEM images

MSc Thesis

Materials Chemistry and Catalysis
Debye Institute for Nanomaterials Science
Utrecht University

G.B. van der Scheer

Daily Supervisors: Dr. T.A.J. Welling & Dr. G.F. Tierney
First Examiner: Prof. Dr. P.E. de Jongh
Second Examiner: Dr. J.E.S. van der Hoeven

June 2023

Layman's abstract

As we are striving to reduce greenhouse gas emissions, such as carbon dioxide (CO_2), we are in need of green energy sources. Hydrogen (H_2) can be used as a CO_2-free source, as combing this with oxygen in electrochemical fuel cells produces electricity and H_2O. H_2 can easily be made from water using a process called electrolysis, however, the total production is not sufficient enough to sustain a H_2-based energy network in the foreseeable future. To help us bridge the gap from fossil fuels to H_2, we can make use of methane (CH_4) to produce H_2. Currently, a lot of H_2 is produced for industry from CH_4 using steam methane reforming, which releases large amounts of CO_2. To avoid this, we can directly break CH_4 into two molecules of H_2 and one carbon atom, without emitting greenhouse gasses. This process is called methane decomposition.

Using heterogeneous catalysts, we can make this process fast and efficient. Heterogeneous catalysis consists of a gas/liquid reactant flowing over a solid catalyst particle. This catalyst particle can lower the activation barriers of reactants and thus promote the fast decomposition of methane into carbon and H_2. Late 3d transition metals such as Nickel (Ni) are highly efficient in this process. To avoid fast deactivation by the Ni particles melting together in a process called agglomeration, particles are deposited on a support material preventing movement. As methane is decomposed on the Ni particle, H_2 and carbon nanofibers (CNF) are formed. The latter happens between the Ni particle and the support material, separating the two and lifting the particle away from the support. These CNFs can continue to grow μm's (a million times smaller tan a meter, 10^{-6} m) long structures and are interesting to industry due to their high mechanical strength and applications such as gas storage and catalyst support.

Earlier research has shown that the choice of support materials can significantly influence the performance of the Ni catalyst. Also, the diameter of the particle, ranging from a few to tens of nm's (10^{-9} m), was found to influence the total carbon production. However, most studies rely on the total performance of the catalysts to determine the optimal support material and particle size. Many different factors such as the geometry of the support and differences in particle sizes make comparisons really hard to make.

In order to exactly visualise what is happening to individual Ni particles during CNF growth, we make use of transmission electron microscopy (TEM). Normal conventional microscopes are limited by the wavelength of light interacting with the object, making the observation of atoms impossible. During electron microscopy, an electron is used instead of light. The wavelength of such a high-energy electron is significantly smaller, allowing us to visualise particles at an atomic scale (10^{-10} m). Using in-situ (literally meaning "in position") TEM we can visualise CNF growth over the Ni catalysts at this atomic scale. This is done by using a specialised gas cell, in which we can deposit our catalysts and expose them to methane. This results in CNF growth which we can then observe directly and make movies of.

In this thesis, we will make use of these in-situ TEM movies and focus on analysing the carbon growth rate from Ni-based catalysts, i.e. how much carbon is grown over a period of time. We will investigate the effect of support material and particle size on the carbon growth rate and how fast the catalyst deactivates. A special approach is needed, as CNFs grow in 3D space and we analyse 2D images. Also as electrons can influence the carbon CNF growth rate, the number of electrons used to visualise the reaction is kept to a minimum, resulting in a low resolution of the movies. Therefore we use a method that aims to exclude most of the errors these factors introduce, while we still try to be aware of these during our analysis.

It was found that the CNF growth rate on individual Ni particles was dependent on the support material, even though there was no direct contact with the support after the initial stage of the reaction. Therefore we discussed that the initiation of the CNFs greatly influences carbon growth rates. Support materials can interact more strongly with the Ni particle, and as a consequence, the Ni particle surface gets covered with carbon. Less of this surface can then decompose methane and thus results in lower CNF growth rates. Additionally, we found that the particle size significantly influences how fast Ni particles deactivate on GNP and

GNP-ox, whereas Ni on SiO_2 and TiO_2 saw no significant particle size dependency. We also observed that the support material influences how steadily CNFs grow. Ni particles on GNP and GNP-ox could suddenly stop after growing CNFs and continue afterwards, while particles on SiO_2 and TiO_2 were continuously growing CNFs. Hypothetically, these differences arose from the different shapes Ni particles had, which depended on the support material used.

Additional experiments, where we tried to regenerate the activity on these Ni-catalysts by exposing them to H_2 were also performed. This would hypothetically make methane of the solid carbon deactivating the Ni-particle surface, which is actually the reverse of our process. We found that regeneration increased the total amount of active particles. However, regeneration in terms of carbon growth rate depended on how severely carbon structures would be affected during exposure to H_2. Nevertheless, it proved to be a promising approach to catalyst regeneration.

This thesis shows how we can analyse the CNF growth from Ni-based catalysts from in-situ TEM movies, to gain a better understanding of the effect of Ni particle size and support material. Still, some future experiments are necessary to validate and help us interpret observations made in the thesis. Nevertheless, this research hopes to contribute to a better understanding of methane decomposition in order to produce H_2 more efficiently.

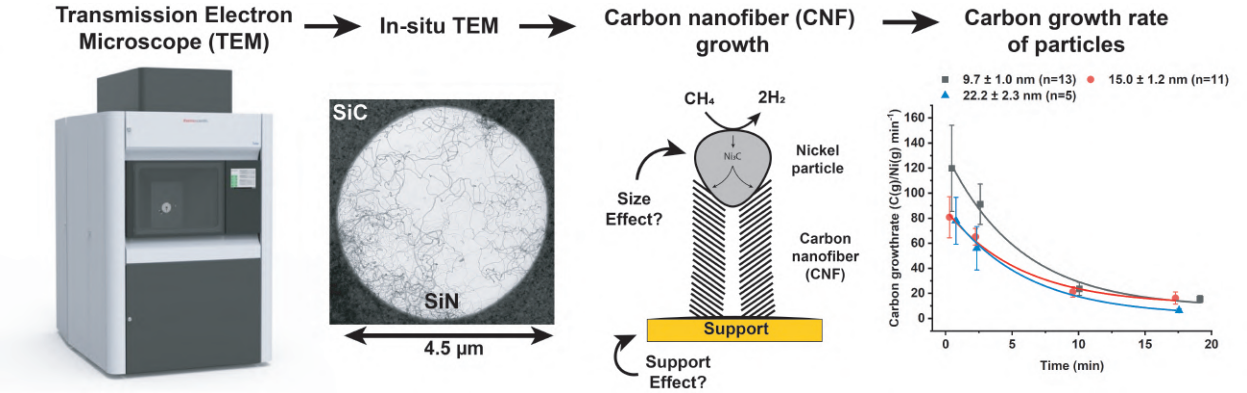

Figure 1: Graphical abstract

Abstract

As the world is transitioning to green energy sources, we are still dependent on the energy that fossil sources such as methane (CH_4) provide us. Making use of methane decomposition over Ni-based catalysts, we can decompose CH_4 into carbon nanofibers (CNF) and hydrogen (H_2) which are of great interest as high-tensile strength material and CO_2-free energy source, respectively. Prior research has shown that the choice of support materials greatly influences the performances of Ni-based catalysts. However, these works were dependent on bulk data which relies on a combination of factors influencing catalytic results, making direct support and particle size comparisons difficult.

In this work, the particle size and support effect during methane decomposition were investigated using gas-cell in-situ transmission electron microscopy (TEM). Using incipient wetness impregnation Ni particles were deposited on different support materials: carbon (GNP), oxidised carbon (GNP-ox), SiO_2, and TiO_2. Catalytic tests were performed (550 °C, 75/25% CH_4/H_2, 1 bar) on these catalysts and image series were obtained using in-situ TEM. An approach was presented to analyse the CNF growth from these images while accounting for the errors this introduces.

This study found that the support material influences the carbon growth rate and deactivation rate of individual particles. Ni supported on GNP and GNP-ox saw fast deactivation of small particles (< 10 nm) and slow deactivation on larger ones (> 30 nm), while Ni supported on SiO_2 and TiO_2 saw no significant particle size dependency. Ni/SiO_2 showed significantly higher carbon growth rates compared to other catalysts. We postulate that this is due to stronger metal-support interactions, which stimulate carbon accumulation at active metal sites. Furthermore, two growth modes were identified and characterised: stuttering CNF growth on Ni/GNP and Ni/GNP-ox and continuous growth on Ni/SiO_2 and Ni/TiO_2. Additionally, regeneration experiments performed by brief exposure of H_2 to the deactivating catalyst proved to be a promising method to regenerate catalytic activity.

Contents

Chapter 1

Introduction

The concentration of greenhouse gases in the earth's atmosphere is raising great global concern. Today's industry is greatly dependent on nonrenewable fossil energy sources and still will be for the foreseeable future. Unfortunately, these sources are accompanied by significant greenhouse gasses (GHGs), such as carbon dioxide (CO_2). Therefore, we are in the race for climate-neutral energy sources. Many advances have already been made in the field of electrocatalysis, wind and solar energy, allowing for green energy production [1]. However, fossil fuels must be used in our transition to a climate-neutral world, as these upcoming technologies are not sufficient yet as stand-alone energy sources. Natural gas, consisting primarily of methane (CH_4), is not only a much-applied energy source in the industry but also for consumer usage. The energy demand is thus greatly dependent on CH_4, and to still use its potential energy without producing GHGs, we must transform it into a CO_2-free energy source like hydrogen (H_2).

H_2 is recognised as a key option to realise the net zero greenhouse gas emissions commitments set by governments. H_2 can be used in fuel cells without emitting unwanted greenhouse gases, but also new steel production projects are starting up after the first demonstration project of the direct fossil-free reduction of iron using H_2 [2] . Also large amounts of H_2 are used during the production of many essential chemicals such as ammonia. In 2021, 62% of the produced H_2 originated from natural gases, using mainly steam methane reforming (SMR) [3]. In this process, CH_4 reacts with water to produce syngas consisting of H_2 and carbon monoxide (CO). When the objective is to produce H_2, CO is subsequently fed to a water gas shift reactor to react with H_2O to produce CO_2 [4].

To synthesise H_2 without producing unwanted CO_2 emissions, the direct thermal decomposition of methane is a promising strategy [5]. This is based on the endothermic decomposition of methane in solid carbon and hydrogen 1.1. To make this process efficient, we can use catalysis to aid decomposition. Catalysis is indispensable in modern society, playing an important role in the fabrication of everyday products such as plastics, fuels, and medicine [6]. Heterogeneous catalysis is based on the catalytic conversion of a liquid or gas over a solid catalyst, lowering the energy barrier to the desired product with high selectivity. Late transition metals (Co-Fe-Ni) have proven to be highly active in promoting the decomposition of methane, of which nickel (Ni) has proven to be the most active to facilitate this decomposition [7]. These metals are often deposited on a support material to increase thermal stability by preventing rapid agglomeration and thus deactivation. When using such heterogeneous catalysts during methane decomposition, one produces not only H_2 but also grows carbon nanofibers (CNFs). Similar to H_2, CNFs can also be utilized in various interesting applications. Due to nanometer-range diameters, they can be applied as catalyst supports [8, 9], for gas storage [10, 11], and also their mechanical properties can be exploited as strong, light, and cheap composite materials [12].

$$CH_4 \rightarrow C* + 2H_2, \;\; \Delta H^0_{25^C} = +74.8 \text{ kJ/mol} \tag{1.1}$$

The performances of these 3d transition metal catalysts are strongly dependent on various properties. Two prominent examples are the particle size of the metal and the choice of support material on which this is deposited. In this thesis, we will focus on the effect of both these factors on Ni-based catalysts. In the upcoming sections, we will discuss the mechanics of methane decomposition over these catalysts and the metal particle size and support effect from the literature. We highlight difficulties in these studies and how we can exclude them by utilising in-situ transmission electron microscopy (TEM). At the end of this chapter, we will present the type of support materials investigated and how similar-sized Ni particles can be deposited on these for in-situ TEM studies.

1.1 Methane decomposition

In order to gain a better understanding of methane decomposition using Ni-based catalysts, a schematic overview can be seen in Figure 3.5. This process consists of three important steps which are methane decomposition, carbon diffusion, and CNF output. The following model is proposed:

1. Methane molecules are chemisorbed at the catalysts' surface and decomposed into solid carbon and H_2. The high activity of Ni can be explained due to partially filled 3d orbitals, which can accept electrons from the C-H bond [13]. This adsorption is preferred on the open step edges Ni(100) and Ni(110) faces, which are deemed to be the most active in decomposing methane [14]. There are two proposed methane adsorption mechanisms: Firstly a dissociative adsorption mechanism, in which methane dissociates upon adsorption into chemisorbed CH_3* and H* fragments [15, 16]. Secondly, a molecular adsorption mechanism is proposed, where methane is adsorbed at the catalyst surface and subsequently dissociates [17]. In both mechanisms, the removal of the first hydrogen from the methane is proposed as the rate-determining step [17]. However, some studies state that the removal of hydrogen from the methyl group might be rate-determining for methane decomposition [15]. After decomposition, the deposited carbon atoms are then dissolved in the bulk of the Ni particle.

2. Carbon atoms are subsequently diffused to the metal-support interface through the bulk of the particle, however, contributions of carbon diffusion over the metal surface cannot be excluded [5, 18]. Bulk diffusion occurs as carbon forms a metastable nickel carbide (Ni_3C) phase upon dissolving[19]. During this, the magnetisation saturation (M_{sat}) was lowered due to an increase in the nonferromagnetic Ni_3C phase [5]. Upon Ni_3C supersaturation, carbon is pushed out of the metal particle at the metal-support interface, consequently growing graphene sheets epitaxially on the Ni(111) facets.
   The driving force of this bulk carbon diffusion is argued to be a Ni_3C concentration gradient from the active sites to the metal-support interface [5, 20]. This is in contrast to larger hydrocarbons, such as ethene, as during these exothermic decomposition's a thermal gradient is the carbon diffusion driving force. Because the decomposition of methane is an endothermic process, no such thermal gradient occurs. According to Fick's Law (1.2), diffusion is dependent on a concentration gradient through the metal particle, in which D is the diffusivity coefficient which depends on the temperature and the material and ∇c is the concentration gradient through the metal particle. Thus, in a well-established equilibrium between carbon deposition and CNF nucleation, the concentration gradient is steep enough to allow for proper and fast carbon diffusion.

$$J = -D\nabla c \tag{1.2}$$

3. Due to the consequent pressure build-up from graphene sheets at the metal-support interface, the Ni particle is elongated. If the increase in Ni surface energy cannot be compensated anymore by the binding of graphene, the particle is contracted to a more spherical shape and separated from the support surface [18]. The metal particle is then lifted away from the support, nucleating CNFs during steady-state growth. This process is called tip-growth, as the Ni particle is located on top of the CNF (Figure 3.5 A). Regarding the structural properties, the resulting CNF consists of turbostatic graphite

of which the diameter is generally accepted to be the same as that of the metal particle [5, 20]. The fiber is classified as having a herringbone-type texture due to the oblique stacking of graphene layers with respect to the axis.

If the interaction between the metal particle and support is strong, a base-growth mechanism can occur (Figure 3.5 B). During this growth, the metal particle is stuck to the support and CNFs nucleate on top of the metal. This growth mechanism is favoured when strong metal-support interactions (SMSI) are present [21] and/or acute contact angles between the metal and support exist [22], inhibiting the lifting of the metal particle from the support. However, in this research, we will mainly focus on CNF formation during tip-based growth.

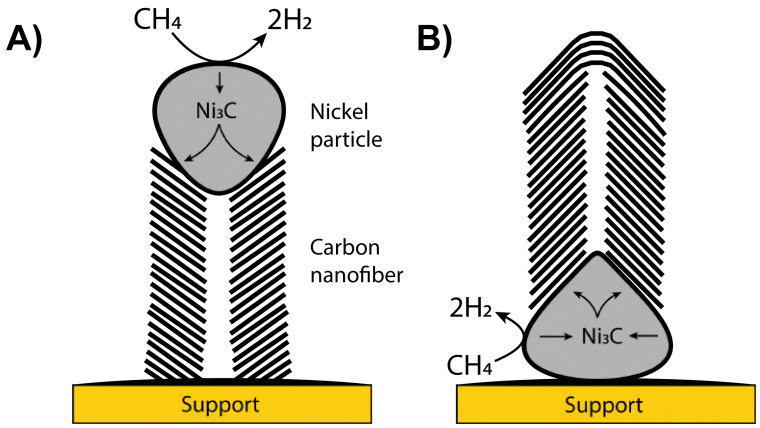

Figure 1.1: A) Tip-growth mechanism. The particle is lifted from the support and grows herringbone-type CNFs in open space. B) Base-growth in which the metal-support interaction inhibits the particle from being lifted, resulting in CNFs growth on top of the particle.

In order to sustain CNF growth, the balance between carbon input, diffusion and output is important. In literature, it is accepted that the main deactivation mechanism is carbon encapsulation. This occurs when deposited carbon does not have sufficient time to migrate through/over the particle. This results in carbon accumulation at the active sites, rendering them incapable of adsorbing methane for further decomposition [5, 13, 23]. Therefore, too fast methane decomposition is undesired. Another deactivation mechanism is caused by the entanglement of particles during CNF growth. This is caused by space becoming limited due to the expansion of the system. However, rational reactor design such as fluidized-bed reactors, can minimize these effects [13].

Reaction circumstances greatly influence CNF yield and morphology. Methane decomposition is an endothermic reaction and therefore favoured at higher temperatures. However, at temperatures too high, methane is decomposed too quickly and carbon diffusion or CNF formation can become the rate-limiting factor. The concentration gradient will flatten out, leading to a lack of deposited carbon diffusion, deactivating the catalyst. Too low temperatures will result in a lack of deposited carbon and low diffusion rates, therefore a temperature range of 500-700 °C is preferred for Ni-based catalysts [24]. Lower temperatures may also promote full CNF as these are thermodynamically more favourable, whereas at higher temperatures kinetically favoured hollow fibers are formed [17, 25].
Methane decomposition is sensitive to pressure. According to Le Chateliers principle, a system will counteract a change in pressure. And since one CH_4 molecule is replaced by two H_2 molecules, resulting in an increase in pressure, the reaction is preferred at low pressures [13]. Since running a reaction below atmo-

spheric pressures has proven to be costly and complex, an inert gas such as Ar or N_2 is often added to lower the partial pressure of CH_4 in the stream [20, 25]. Using this, Ashik *et al.* found optimal CNF yields over Ni/SiO_2 catalysts at a partial methane pressure of 0.8 atm, as lower partial pressures result in a lack of carbon production [26]. Additional H_2 can also be added to the reactants, which will initially reduce activity as the equilibrium is shifted more towards the formation of methane. However, adding H_2 has proven to prolong the catalytic lifetime significantly by removing accumulating carbon from the active sites, reducing deactivation rates [20, 27].

1.1.1 Metal particle effects

The metal particle properties are important as imbalances in the carbon input, diffusion and CNF growth can result in quick deactivation. To improve performances, a wide variety of research has been done regarding the promotion of these metals, obtaining high carbon yields [28]. For example, Cu-promoted Ni particles allowed for better carbon diffusion and gave a variety of CNF structures [25, 29]. Nevertheless, in this thesis, we will only make use of unpromoted Ni as our metal catalyst and study the particle size effect.

During earlier experiments in our group, we found that Ni particle sizes < 7 nm hardly nucleate fibers. Above this size limit, traditional particle size effects like an increase in step edges are negligible [30]. Also, variations in the strength of metal-support interaction (MSI) depending on particle size are expected to be nihil, as Liang *et al.* found no differences between 11 and 24 nm Ni particles on MgAl supports using XPS studies [31]. Therefore the most prominent difference between various nanoparticle sizes is the relative surface-to-volume ratio. Smaller particles have a relatively large amount of surface area, resulting in a large quantity of deposited carbon. The lower particle size limit is thus a result of an excess of deposited carbon that cannot be diffused quickly enough. With increasing particle size, the surface-to-volume ratio is decreased. This means that larger particles have a relatively low amount of carbon deposited compared to smaller particles and the larger size limit is due to a lack of deposited carbon to sustain CNF growth. A well-established balance between carbon input, diffusion and output is thus essential for obtaining high H_2 and CNF yields.

Multiple studies investigated the optimal Ni particle size for methane decomposition. Baker *et al.* found that a decrease in nanoparticle size resulted in a higher rate of CNF formation (in nm s^{-1}) [32]. Chen *et al.* studied the decomposition of Ni on hydrotalcite (HT) and found that particles between 10 and 100 nm had similar initial activity. They compared different particle sizes on variations of HT and found that 34 nm particles resulted in the highest CNF yield at 580 °C[20]. They argued that the lower size limit is due to an increased carbon concentration in the particle, flattening the carbon concentration gradient. The upper size limit is assigned to a lack of surface area. Takenaka *et al.* found that optimum yield was dependent on the Ni loading on SiO_2, in which they assigned the cause to an optimum in Ni particle size of 60-100 nm [33] at 500 °C. Ermakova *et al.* showed an optimal Ni particle size range of 10-40 nm on SiO_2 at 550 °C [34]. Lastly, Li *et al.* synthesised unsupported Ni crystallites with ethylene glycol as a mediator and produced relatively high carbon yields. They determined an optimum in H_2 and CNF yields in Ni particles with a 10.8 nm crystallite size and total deactivation of particles above 26 nm at 500 °C.
Different optimal Ni particles sizes ranging from 10 to 100 nanometers are thus suggested. However, particle size comparisons are difficult as other factors like temperature and the choice of support materials can significantly influence bulk performance.

1.1.2 Metal-support interactions

Previous research revealed that H_2 and CNF yields differ significantly over various supports in Ni-based catalysts [7, 34–37]. The support pore volume, pore size and surface area play an essential role, as these will allow physical space for the CNFs to grow over time. Takenaka *et al.* showed that the yields of Ni supported on silica (SiO_2) are greatly dependent on the pore structure, as limited space resulted in CNF

entanglement and quick deactivation [35]. Therefore support materials without pores were argued to show the least deactivation.

Metal-support interactions (MSI) significantly influence the properties of catalysts in terms of metal size, distribution, and reducibility. High surface areas influence particle sizes as precursor species are distributed over a larger surface area. Also, the composition in terms of surface group density is important, as oppositely charged metal precursors interact with charged surface groups. High densities will thus enhance the distribution of metal precursors and thus lead to smaller particles. This increase in surface groups will also interact more strongly with the metal nanoparticle, inhibiting lifting off and/or movement over the support surface [38]. A strong MSI can increase the reduction temperature of the metal oxide or even produce hard-to-reduce strong metal-support interactions (SMSI). These SMSI refer to suboxides that can cover the metal particle surface [39] and drastically reduce the performance of the catalyst by blocking active sites. Furthermore, these species can inhibit carbon diffusion [40] and prevent the metal particle from lifting from the support. One should thus prioritize the prevention of these species while using metal oxide supports.

Traditional metal-support interactions consist of factors such as charge transfer, interfacial perimeter, and metal particle morphology changes and can significantly influence the catalytic performances [41]. However, as particle sizes above 6 nm are used, these interactions are expected to have a negligible effect on the direct kinetic properties of the decomposition of methane. Nevertheless, the atoms at the metal-support interface where CNFs nucleate are directly influenced by these factors. These may provide an (dis-)advantageous environment for the nucleation of CNFs, which can influence the CNF growth rate depending on the support material used. Li *et al.* increased the MSI on Co/SiO_2 catalysts by implementing BaO, La_2O_3, and ZrO_2 to a SiO_2 support. What they concluded is that the deactivation rate increased with an increasing MSI. This was assigned to a stronger MSI hindering the lifting of the particle and therefore CNF formation. As a result, the carbon concentration gradient flattens out and carbon cannot be diffused away quickly enough, followed up by carbon accumulation on the active sites [37].

Numerous studies have discussed the support effect during methane decomposition using Ni catalysts. Here we will quickly run down some prominent ones. Takenaka *et al.* prepared catalysts using incipient wetness impregnation and found that Ni/TiO_2, Ni/graphite, and Ni/SiO_2 showed to be the most effective catalysts for methane decomposition [35]. Ni/SiO_2 showed the highest carbon yield and as mentioned earlier they argued that pore volume and size was the most important factor in obtaining high carbon yields. Ni/MgO, Ni/Al_2O_3 and $Ni/MgO\text{-}SiO_2$ did not nucleate fibers, which was assigned to the absence of the metallic Ni phase. Furthermore, Ermakova *et al.* added metal oxides to NiO as a textural promoter and showed that Ni/SiO_2 produced the highest carbon yield [34]. Rastegarpanah *et al.* prepared catalysts by a "one-pot" evaporation self-assembly strategy and concluded that Ni/MgO had the highest CNF yield. However, the big difference in nanoparticle size between supports is likely the cause of this observation [36], as they compare 4 nm particles on SiO_2 with 29.0 nm particles on MgO.

Selecting an optimal support material is thus essential in obtaining high carbon yields. Importantly, all of these mentioned studies regarding support and particle size effect, rely on data from bulk catalysts. This is an accumulation of all active and inactive particles with various sizes supported on materials with different pore sizes and interactions with the Ni particle. These factors significantly complicate comparisons during methane decomposition since it is often assumed that bulk kinetics directly correlate to individual particle kinetics, leading to disputes in the literature.

1.2 In-situ TEM

1.2.1 Transmission electron microscopy

In-situ transmission electron microscopy (TEM) provides us with a unique opportunity to investigate these support and particle size effects at a single particle level with high spatial resolution. As we can operate under the same conditions as the ex-situ catalytic experiments, we can image the formation of CNFs in real time. This enables one to directly compare Ni particles of various sizes in similar positions on different supports, making comparisons as honest as possible.

TEM is of great importance in materials science as it allows us to image the formation of these CNF materials at atomic resolutions [42]. In microscopy, the resolution (d) is proportionate to the wavelength (λ) of the interacting particle (1.3). In electron microscopy, the wavelength is determined by the kinetic energy of an electron (1.4), in which h is Planck's constant, m_0 is the electron mass, e the electron's charge, and V the acceleration voltage of the electron. As a result, typical 200 kV acceleration voltages in TEM can theoretically achieve a spatial resolution of 2.5 pm. However, the real resolution limit is due to inhomogeneous electron sources and beam optics. Chromatic aberration C_c is a result of a not perfectly monoenergetic electron beam, resulting in a spread of electron energies thus lowering the resolution. Spherical aberrations C_s are due to imperfections in the magnetic optics, distorting the signal. Nevertheless, advances in aberration corrections have tremendously increased resolutions and will continue to do so.

$$d = \frac{\lambda}{2NA} \tag{1.3}$$

$$\lambda = \frac{h}{(2m_0eV)^{1/2}} \tag{1.4}$$

As we will operate in regular TEM mode, the direct electron beam intensity is measured on a charge-coupled device (CCD). The incident image is thus a projection of the sample. Origins of contrast are important to understand as it provides information regarding the sample. Mass-thickness contrast is dependent on the sample thickness and material-dependent cross-section. This can help us differentiate the Ni particle, CNF and support. Diffraction contrast is dependent on crystalline materials diffracting electrons, which can give information regarding the orientation of crystalline domains.

1.2.2 In-situ TEM

Due to significant advances in the field of microchip fabrication, microchips with thin (30-50 nm) SiN windows are now available commercially. These allow us to images sample in liquid or gaseous environments that are shielded from the vacuum of the microscope, without drastic decrease of the resolution [43]. Real-time dynamic changes during methane decomposition can thus be imaged at industry-relevant pressures and temperatures. Methane decomposition has previously been studied using environmental in-situ TEM, which allows the sample to be exposed to a maximum of 20 mbar of reactants pressure. Most noticeably Helveg *et al.* performed an in-depth study regarding the growth dynamics of CNFs during the nucleation phase [18]. Focusing on the growth and nucleation of graphene sheets on the Ni surface, which are to be assisted by the dynamic restructuring of the metal step edges. Lyu *et al.* studied the dynamic circles of the Ni_3C particle shape during CNF formation [19]. However, one should note that these measurements were performed at low pressures (2.0 mbar). Due to the notorious pressure gap, nanoparticles may behave differently at low pressures, exposing other facets and altering the methane decomposition activity and/or CNFs formation mechanics. Furthermore, electron beam irradiation is a non-negligible effect during in-situ TEM experiments. Experiments by Helveg *et al.* and Lyu *et al.* were performed under high electron doses, as the former performed theirs at >124 e^- $Å^{-2}$ s^{-1}. As a result, electron-gas (ionization of gas molecules) and electron-material interactions may significantly alter the electronic properties and activity of the catalysts, and thus lead to inconsistencies compared to ex-situ results. Our experiments will consider the influence of

pressure gaps and electron beam effects by operating at atmospheric pressures and low electron doses. While this approach may lead to lower resolutions compared to previous studies, it is deemed the most equitable.

As opposed to Helveg *et al.* and Lyu *et al.*, we will focus on the volume of CNFs that is grown, instead of CNF formation mechanics. This gives us direct information regarding the activity and deactivation of catalyst particles in terms of carbon growth rate. A schematic overview of the in-situ TEM gas cell is shown in Figure 1.2. The gas cell consists of two microchips with electron-transparent windows which are stacked above and under the deposited catalysts, which seal off the gas atmosphere from the TEM column. One chip contains gold electrodes connected to a thin, durable silicon carbide-based ceramic thin film heating membrane, allowing for quick heating and cooling (10^6 °C s^{-1}) . This area also contains 6 small amorphous, electron-transparent SiN ($\leq$ 50 nm thick) windows to image the sample (Figure1.2 A). Another chip consists of silicon with a relatively large SiN window in the middle. Combining two of these chips results in a complete gas cell (Figure1.2 B).

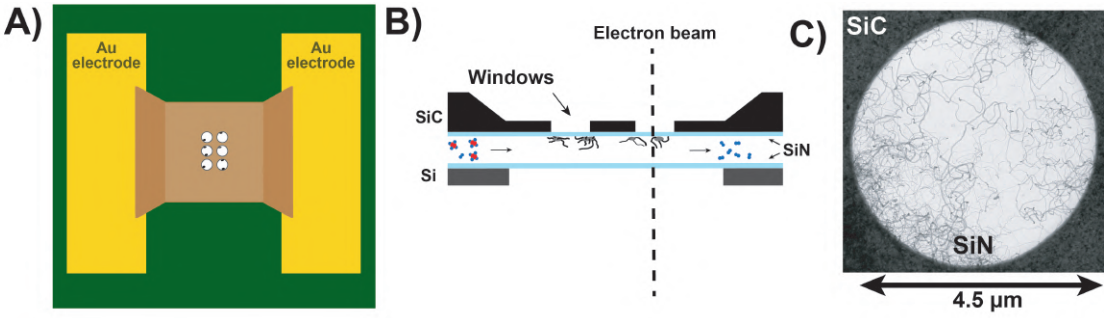

Figure 1.2: Schematic overview of in-situ TEM chip. (A) The chip is heated by 2 gold electrodes which are connected to a thermally conductive SiC plate. (B) Holes in this SiC allow for the electron beam to pass through while SiN windows seal the gas off from the TEM column. (C) CNF growth can be visualised through these windows.

In order to gain a better understanding of the in-situ TEM system and therefore its limitations, a schematic overview is presented in Figure 1.3. The 'system' refers to all gas lines including the holder and storage tanks. Up to three different gases can be used simultaneously during experiments, which are stored as a reaction mixture in two separate storage tanks. These tanks allow for a controlled flow rate to the holder for a sustained period of time (>1 hour). In order to change the gas flow through any of the lines, the system is evacuated using a vacuum pump (as low as 1 bar). For example, if one wants to switch the atmosphere in the holder from a reducing atmosphere which was stored in 'Storage Tank 1' to the reaction atmosphere in 'Storage Tank 2', all lines between the storage tank and holder and the holder itself are pumped down to low pressure. This results in low pressures around the sample. Before and after experiments, the system has to be 'pump-purged'. This is a process in which Ar fills the lines and is evacuated for multiple cycles. This is done in order to remove any contaminations from the gas lines and has proven essential for successful experiments.

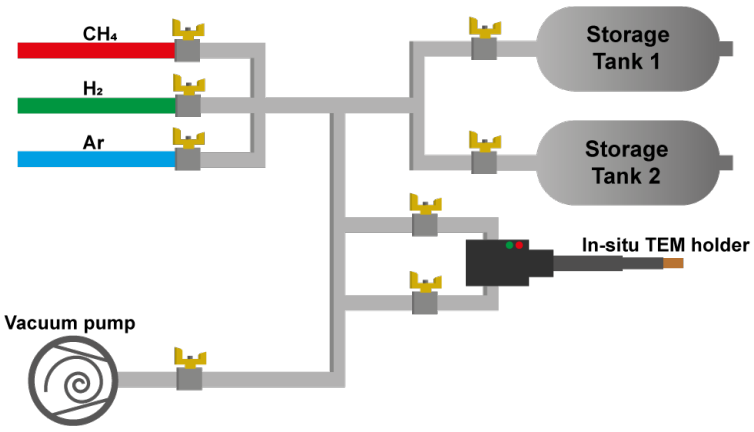

Figure 1.3: Schematic overview of in-situ TEM system. Valve switches are placed between every object in the system and can be closed depending on the preferences.

1.3 Catalyst synthesis

1.3.1 Investigated support materials

As previously stated, the present study aims to investigate the CNFs on various support materials. In order to provide an overview of the properties associated with these materials, we will now introduce them in this section.

1. Graphene nanoplates (GNP, xGnPC-500) is a high-purity carbon material with a high surface area of approximately 500 m^2 g^{-1} and a pore volume of 0.9 mL g^{-1}. These materials consist of stacked turbostatic graphene sheets and a great advantage is their relative inertness compared to metal oxide supports. Nevertheless, defects in its structure are prone to interact with oxygen, which introduces active surface groups [44]. These acidic surface groups will influence the precursor distribution and interact with the active Ni particle. Furthermore, as carbon is a light material the contrast with Ni is larger, which makes in-situ TEM studies easier to analyse.

2. Oxidised Graphene nanoplates (GNP-ox) is used as support material in order to test the influence of the number of surface groups interacting with the particle during methane decomposition. One can increase their respective density using an oxidation treatment. Liquid phase oxidation using nitric acid (HNO_3) as an oxidizing agent is a well-known method to realise this. By suspending the carbon material in the acid solution, a wide variety of acidic oxygen-containing surface groups are introduced, including mainly carboxylic, lactone, and phenolic hydroxyl groups [45]. However, these oxygen-containing groups are known to be sensitive to thermal decomposition at catalytic temperatures [46]. By altering the acid concentration and the duration of the synthesis, one can control the number of surface groups introduced. A big disadvantage of this treatment is the severe structural damage it introduces to the support.

3. Silica (SiO_2, Aerosil380) has proven to be one of the more effective catalyst support in previous research [34, 35]. This fumed silica is an amorphous semiconductor material with an estimated surface area of 380 m^2/g and pore volume of 0.9 mL/g. Silica as support is stable, as the Si^{4+} state is hardly reducible. Surface groups mainly consist of acidic silanols and siloxanes [47].

4. Titania (TiO_2, aeroxide P90) is a relatively low surface area ($\sim$ 81 m^2) semiconductor material. It is often used in photocatalysis, however, it can also be applied as support material during methane decomposition. TiO_2 (aeroxide P90) is crystalline and consists of approximately 80/20 anatase to rutile phases. Surface groups consist mainly of hydroxy groups and oxygen bridges with a slightly

acidic nature [48]. One should avoid the formation of $NiTiO_3$ species, as these SMSI can migrate to active surface sites and inhibit carbon diffusion[39, 40].

5. Magnesia (MgO, powder -325 mesh) is a basic ceramic material, often used for electronic applications as filler material due to a high volumetric resistivity (10^{17} Ω·m) and wide band gap (7.8 eV)[49]. The estimated pore volume is around 0.25 mL/g and with a surface area of 150 m^2/g. Due to its hygroscopic properties, MgO forms $Mg(OH)_2$ in aqueous solutions which can significantly alter the support structure upon impregnation. Upon drying the support, the water is removed and the MgO phase is restored. MgO can be dissolved in an acidic aqueous solution therefore basic precursor solutions are preferred. As an increase in $Ni(NO_3)_2{\cdot}6H_2O$ concentration lowers the pH of the solution, the solubility of the MgO increased. Therefore concentrations are preferably kept to a minimum, while still operating at high enough weight loadings for sufficient particles during in-situ TEM studies.
Alternative precursors could be used to avoid these unwanted effects. Other ligands, like the commonly used nickel chloride or nickel acetylacetonate, can be dissolved in non-aqueous solutions. However, varying these can significantly influence catalytic properties in terms of metal-support interactions and poisoning [50]. Therefore, in order to keep support comparisons fair, nickel nitrate hexahydrate is preferred to exclude possible precursor effects.

1.3.2 Incipient wetness impregnation

In order to deposit Ni particles on these support materials, the incipient wetness impregnation (IWI) approach is used, see Figure 1.4. As this method is well understood, it allows us to alter the catalyst's properties by changing specific parameters. All catalysts in this thesis are synthesised using a highly soluble nickel nitrate hexahydrate salt ($Ni(NO_3)_2{\cdot}6H_2O$). By altering the concentrations of this precursor solution, one can get the desired weight loading on the support material. Weight loadings can be varied if one would like to adjust final Ni particle sizes. Logically, higher weight loadings usually lead to larger particles whereas lower weight loadings lead to smaller metal particles. Normally, variations in weight loading result in different gas hourly space velocities (GHSVs) between catalysts, affecting yield. However, in-situ TEM experiments are operated with only femtograms of the sample in the gas cell, with high gas flows (0.1 - 1 sccm). This results in high GHSVs and variations in the weight loading should not affect catalytic performances during comparison.

During IWI, a metal-containing precursor is added to the porous support. In order to maintain a solid support state, the precursor volume is always less than the total pore volume of the support. As a result of this, weight loadings are determined by the pore volume of the support when impregnating similar precursor concentrations. Upon adding the metal precursor, the solution will enter the pores by capillary forces. One should be aware of the hydrophilic/hydrophobic nature of the support material, as this will provide the wetting of the support surface, which is essential for fine metal particle dispersion. When aqueous solutions should be avoided, like with hygroscopic MgO which forms $Mg(OH_2)$ in aqueous solutions, ethanol can be used as a precursor solvent. This will also promote a finer dispersion over the support [51]. During impregnation, the pH of the aqueous metal precursor solution should be lower than the point of zero charge (PZC). This will facilitate the adsorption of anionic precursor groups by positively charged surface groups. However, too strong interactions can inhibit fine dispersion, resulting in egg-shell precursor distributions. Therefore a balance between adsorption and diffusion is necessary to obtain a uniform distribution [52]. The precursor solvent is subsequently removed from the support using vacuum drying, as metal precursors are bound to the support using electrostatic interactions.
Dried materials will undergo a heat treatment, in which precursors migrate over the support surface. In the case of $Ni(NO_3)_2$, the precursor is decomposed stepwise into NiO under an N_2 atmosphere. A great advantage of this approach is that it leaves no impurities behind [53]. Adjusting the parameters of this heat treatment is an easy method of obtaining a preferred nanoparticle size. For example adding a small percentage of NO to the gas flow results in a more gradual thermal decomposition, which results in a finer metal particle distribution [54]. Whereas temperatures and heating ramps can also be increased for larger Ni particles due to faster migration.

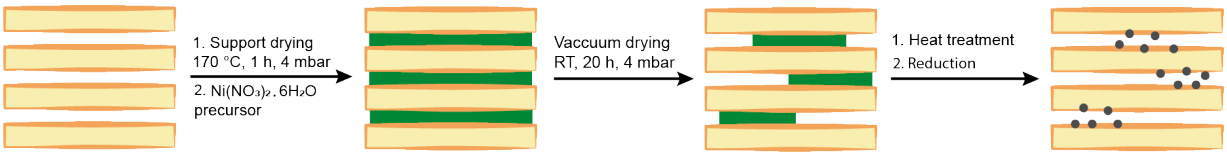

Figure 1.4: Schematic overview of the preparation of Ni-based catalysts via incipient wetness impregnation, followed by the drying to eliminate the solvent, heat treatment to decompose $Ni(NO_3)_2$ into NiO, and the final reduction treatment to create metallic Ni particles.

1.4 Research goals

The aim of this research is to synthesise similar-sized Ni particles on different supports. Consequently, we investigate the CNF growth over these catalysts during methane decomposition using in-situ TEM. Supports that are discussed include:

1. Graphene nanoplates (GNP, xGnPC-500).
2. Oxidized GNP (GNP-ox) using a liquid phase HNO_3 oxidation treatment.
3. Silica oxide (SiO_2, Aerosil380).
4. Titania (TiO_2, P90).
5. Magnesia (MgO, powder -325 mesh).

Using in-situ TEM, we separate factors such as particle size polydispersity, particle dispersity, and support geometry which significantly influence the catalytic activity and deactivation. Due to low resolutions during in-situ TEM experiments with low electron dose rates, we will focus on the amount of carbon that is grown per Ni particle rather than the CNF formation mechanics. This results in the following research questions:

- What is the influence of nanoparticle size on the formation/deactivation rate of CNFs?
- What is the influence of the support on the formation/deactivation rate of CNFs?

In-situ TEM experiments were performed at 550 °C under an 3:1 CH_4:H_2 (1 bar) atmosphere, which are industry-relevant conditions[13]. Additionally, we performed several trials on deactivating catalysts, where we introduced a reducing atmosphere for a brief period of time. Hypothetically this removes encapsulating carbon from deactivated Ni sites, increasing activity. We will label these experiments as "H_2-pulsing".

Upcoming in Chapter 2 we will cover the experimental procedures extensively. This includes the synthesis/characterisation of the catalysts, in-situ TEM experiments, and in-situ TEM image analysis. In Chapter 3 the properties of the synthesised catalysts and in-situ TEM experiments are discussed. In Chapter 4 we will end with a conclusion and an extensive outlook regarding future experiments necessary to complement the results of this thesis.

Chapter 2

Experimental

2.1 Ni-based catalysts synthesis

Nickel(II) nitrate hexaydrate ($Ni(NO_3)_2{\cdot}6H_2O$, $\geq$ 97%), Magnesia (MgO, $\geq$99%, -325 mesh) were purchased from Sigma Aldrich. Nitric acid (65% HNO_3) was purchased from VWR International. Titania (TiO_2 aeroxide P90) was purchased from Degussa. Silica (SiO_2 Aerosil380V) was purchased from Evonik Industries. Graphene nanoplatelets (xGnPC-500, referred to as GNP) were purchased from XG Sciences.

2.1.1 Precursor solution

Catalysts were prepared via incipient wetness impregnation using $Ni(NO_3)_2{\cdot}6H_2O$ precursor solutions. Precursors solutions were prepared by dissolving the desired amount $Ni(NO_3)_2{\cdot}6H_2O$ in a solvent. The pH of the solutions was adjusted to pH $\sim$ 1 by adding 65% HNO_3. The precursor densities were determined from the average of 10 individual density measurements. The studied catalysts, Ni supported on GNP/GNP-ox/SiO_2/TiO_2, were prepared by using a 4 M $Ni(NO_3)_2{\cdot}6H_2O$ in H_2O precursor solution. Next to this 4 M precursor solution, MgO was also impregnated with another precursor was prepared by dissolving $Ni(NO_3)_2{\cdot}6H_2O$ in ethanol, without the addition of 65% HNO_3.

2.1.2 Impregnation and drying

Support materials were vacuum dried at 170 °C prior to impregnation. The precursor was then subsequently added under a vacuum using a syringe of the desired volume. To ensure no overfilling of the supports, 90% of the physisorption determined single point pore volume was impregnated. This was with the exception for MgO, of which the pore volume was determined by the slow addition of ethanol in ambient air under vigorous stirring instead of physisorption. This was done in order to obtain a higher pore volume value. After impregnation, the supports were stirred for 1 hour before being left to dry overnight under a dynamic vacuum to remove the solvent.

Ni/GNP and Ni/GNP-ox were double impregnated with 4 M $Ni(NO_3)_2{\cdot}6H_2O$. The first impregnation was done as described above and the sample was heat treated according to subsection 2.1.3. The single point pore volumes of the resulting NiO/GNP and NiO/GNP-ox were determined using physisorption. These NiO/GNP and NiO/GNP-ox were then vacuum dried at 170 °C and impregnated a second time with the exact same procedure described above. The exact details of the impregnation of all investigated catalysts are presented in Table S5.2.

2.1.3 Precursor decomposition and activation

Impregnated samples were added to a quartz reactor and heat treated at 300 °C (Ni/GNP and Ni/GNP-ox), 350 °C (Ni/MgO), 450 °C (Ni/TiO_2) and 500 °C (Ni/SiO_2) for 2 h under 200 mL N_2 min^{-1} g_{cat}^{-1}. This resulted in the stepwise decomposition of $Ni(NO_3)_2$ precursors into NiO. To reduce particle sizes, 5% NO in N_2 was added to the gas flow of Ni/SiO_2, Ni/TiO_2 and Ni/MgO. Afterwards, all catalysts were reduced at 350 °C (Ni/GNP and Ni/GNP-ox) or 450 °C (Ni/SiO_2) or 550 °C (Ni/TiO_2, Ni/MgO) for 2 h in 10% H_2 in N_2 (300 mL min^{-1} g_{cat}^{-1}). After reduction, the particles were passivated in ambient air.

2.2 Oxidation of GNP-500

Liquid phase oxidation treatment was used to introduce oxygen surface groups to the carbon support. 10 grams of GNP-500 was added to a 1 L round-bottom flask connected to a reflux cooler. The carbon was dissolved in 400 mL of 65% NO_3 and slowly heated to 80 °C and kept on an isothermal hold for 2 h under vigorous stirring. Formed NO_x gasses were led through two washing bottles and subsequently in the fume hood. After heating, the suspension was quenched with 5 L demi water and decanted when the black carbon material had precipitated. This washing step was repeated 5 times until the pH was $\sim$ 6. The decanted black carbon material was then oven-dried at 120 °C for 40 hours and milled into a powder material.

2.3 Characterisation of catalysts

2.3.1 N_2 physisorption

Nitrogen physisorption at 77 K was performed on a Tristar II plus apparatus (Micrometics) to characterise the surface area, pore volume, and pore size of the different supports. Prior to measuring, the samples were dried at 170 °C for 14 hours under a dynamic vacuum. The total pore volume was determined by the adsorption at p/p_0=0.995. The Branauer-Emmet-Teller (BET) surface area was determined in the relative pressure range of p/p_0=0.03-0.014. Pore size distributions were determined using the Barret-Johner-Halenda model.

2.3.2 Support mass titration for determining the point of zero charge

Mass titration was applied to determine the point of zero charge (PZC) of support materials. Increasing amounts of support material were added to 10 mL of 0.1 M KCl under stirring, with 5 minutes in between each step in order for the suspension to stabilize. When the pH did not change as a function of adding material, it was assumed that this pH was equal to the PZC. This is based on the amphoteric behaviour of these support materials.

2.3.3 Titration for determining acidic and basic surface groups

The density of surface groups was determined by potentiometric titration using a Metrohm 888 Titrado setup. Approximately 25 mg of material was suspended in 65 mL 0.1 M KCl under vigorous stirring. Depending on the nature of the surface group 0.01 M HCl (basic) or 0.01 M NaOH (acidic) in 0.1 M KCl was added dropwise to the suspension. The equivalence point of the resulting titration curve (pH as a function of volume added) was considered to be equal to the number of surface groups. The surface group density (#groups nm^{-2}) was calculated using the determined BET surface area from N_2-physisorption according to (2.1).

$$\text{Surface group density}(\#\text{groups}/\text{nm}^2) = \frac{\text{Added NaOH (mol)}}{\text{BET surface area (nm}^2\text{)}} \tag{2.1}$$

2.3.4 Temperature-programmed reduction

Temperature-programmed reduction (TPR) was used to determine the reduction behaviour of NiO on different supports, using a thermal conductivity detector (Micromeritics Autochem II chemisorption analyzer). An oxidation pre-treatment (Table 2.1) was performed on the samples to ensure full oxidation of the NiO species on supports. All samples were sieved in >38 μm fractions before being loaded in a quartz U-type sample tube on top and topped off with quartz wool. Prior to measurements, samples were dried at 120 °C under Ar flow (40 mL STP min^{-1}) for 15 min. Measurements were performed using 5% H_2 in N_2 (40 ml STP min^{-1}). Temperature programs varied between measurements and are described in the caption of each TPR plot.

Table 2.1: Oxidation treatment of heat treated catalysts for TPR analysis.

Time (min)	Temperature (°C)	Ramp (°C min^{-1})	N_2 (ml min^{-1} g_{cat}^{-1})	O_2 (ml min^{-1} g_{cat}^{-1})
10	30	1	190	10
170	200	1	190	10
120	200	1	170	30
999	10	10	20	0

2.3.5 Powder X-ray diffraction

Powder X-ray diffraction (XRD) was performed in order to identify the crystalline phases and crystallite sizes of the samples. Measurements were performed on a Bruker D2 Phaser 2nd Generation diffractometer equipped with a Co-$K_{\alpha 1,2}$ radiation source (λ = 1.7889 Å) with a V20 variable slit. Diffractograms were measured over a range of $2\theta = 15$ - 90° with a 0.02 increment size and 1 sec per measurement time. Diffraction peaks for Ni and NiO are listed in Table 2.2 [55]. Crystalline sizes (d_{XRD}) were measured using the Scherrer equation on a non-overlapping NiO diffraction peak according to (2.2). In which K is the shape factor, β the full width half maximum (FWHM), λ the X-ray wavelength, and θ the Bragg angle.

$$d_{\mathrm{XRD}} = \frac{K\lambda}{\beta cos(\theta)} \tag{2.2}$$

The fraction of the rutile crystalline phase in TiO_2 P90 was determined using the Spurr and Myers equation (2.3). The anatase (101) peak intensity (I_A) at ($\theta = 29°$) and rutile (110) peak intensity (I_R) at ($\theta = 32°$) were used[55].

$$f_R = \frac{1}{1 + 1.265\frac{I_R}{I_A}} \tag{2.3}$$

Table 2.2: XRD peak position for Ni and NiO according to the International Centre of Diffraction Data [55].

Peak position (2 Theta)		
Matal	Angle (°)	Miller Indices
Ni	52	(111)
	61	(200)
	92	(220)
NiO	44	(101)
	51	(012)
	74	(110)(104)

2.3.6 Characterising transmission electron microscopy

Transmission electron microscopy (TEM) was used to characterise particle size and the dispersion of reduced and oxidised catalysts. This was done using a Tecnai 20 (FEI) microscope operated at 200 kV. Samples were loaded onto a holey carbon-coated Cu grid (Agar mesh 200). At least 200 supported particles on different parts of the grid were measured in order to get a representative size distribution. The average nanoparticle size (d_n) was calculated using (2.4).

$$d_n = \frac{1}{N}\sum_{i=1}^{N} d_i \tag{2.4}$$

The standard deviation (σ_s) within the particle size was determined using (2.5), in which (d_i) is the particle diameter and d_μ is the average particle diameter.

$$\sigma_s = \sqrt{\left(\frac{1}{N-1}\right)\sum_{i=1}^{N}(d_i - d_\mu)^2} \tag{2.5}$$

2.4 In-situ TEM experiments

2.4.1 Sample preparation

In-situ TEM experiments were performed using the Atmosphere 210 gas-cell system (Protoschips Inc, USA). To prepare the cells, ex-situ prepared catalysts were dispersed in ethanol. The suspensions were subsequently sonicated for 5 minutes. 1 μL droplets were drop casted on the heating chip containing the 6 windows until sufficient particles were present around the windows, this required approximately 10-30 droplets. The heating chip was then placed on top of the gasket in the pocket. Subsequently, the larger silicon chip containing the large SiN window was placed on top of the heating chip. The holder was then closed using the lid, which was then leak checked under vacuum ex-situ. If no leaks were detected, the holder was inserted in the TEM. Electrical and gas lines were then attached to the holder and no leak was detected if the vacuum of the TEM column did not react. At least 6 pump-purge cycles (300 mbar down to 1 mbar) with Ar were performed throughout the system and holder to remove any contaminations.

2.4.2 Catalytic tests

Prior to the experiments, samples were dried in-situ under Ar at 150 °C for 5 min. Subsequently, catalysts were reduced again in-situ for 1 hour in 10% H_2/Ar at their respective ex-situ reduction temperature (see Table 3.2). The system was then pumped down to a vacuum while raising the temperature to 550 °C. At this temperature, the sample was exposed to the beam and a 3:1 CH_4:H_2 atmosphere was introduced to start the experiment. All atmospheres were introduced at 1 bar with a flow rate of 0.1 sccm. All gases were of purity grade N7.0.

2.4.3 H_2-pulse

During "H_2-pulse" experiments, 10% H_2/Ar was introduced for a brief period of time (typically 30 s) at 550 °C when the catalyst was (partially) deactivated. After this H_2-pulse, the reaction atmosphere of 3:1 CH_4:H_2 was reintroduced. All atmospheres were introduced at 1 bar with a flow rate of 0.1 sccm. Two different approaches to H_2-pulse experiments were taken. First, due to the design of the system, it had to be pumped down to a vacuum before introducing different atmospheres. To prevent this, H_2-pulse experiments were performed where the holder was opened and closed physically in between introducing different atmospheres. As a result, the pressure in the cell was maintained at 1 bar total pressure with a flow rate of 0.0 sccm. Additionally, conventional H_2-pulsing experiments were performed where the system had an intermediate vacuum period. These experiments are addressed with H_2-Vac and H_2-noVac.

2.4.4 In-situ TEM image settings

In-situ TEM experiments were performed on a Talos F200X (200kV acceleration voltage) in TEM mode. Previous experiments in our group tested the beam effects on CNF growth. As a result, we opted to keep electron dose rates $\leq$ 13 e^- $Å^{-2}$ s^{-1}. The electron dose rates were determined by measuring the screen current in the TEM without the sample holder present or any objective apertures inserted, using (2.6). Where A_{screen} is the current of the beam on the fluorescent screen in ampère, e is the charge of an electron, and r_{beam} is the beam's radius. Since our resolution was dose limited, we opted to record image series with a pixel size of approximately 1 nm. The resulting images were 1k by 1k or 2k by 2k pixels, depending on the size of the imaged catalyst particle. Image series were recorded with an integration time of 1-2 seconds per frame. The recording was stopped when 250-300 frames were acquired in order to keep it within a reasonable file size. Multiple image series were made over a 30-50 minute period.

$$\text{Dose rate} = \frac{A_{\text{screen}}}{e * \pi * r_{\text{beam}}^2} = e^- \mathring{A}^{-2} s^{-1} \tag{2.6}$$

2.5 Image analysis

2.5.1 Carbon nanofiber growth

Images were analysed using ImageJ v1.54 [56]. CNFs were measured, depending on the growth speed, every 1 to 3 frames (Figure 2.1 A). CNFs were selected for analysis if particles were:

1. Anchored to one point in order to measure the fiber length from this point to the Ni particle.
2. In focus while growing.
3. Did clearly not grow in the z-axis.
4. Were growing outside the support where they were clear to distinguish from the bulk.

While we are aware this may introduce some bias, this was the only way to reliably measure CNF growth.

As we made 3D assumptions from relatively low-resolution 2D TEM projections, several assumptions were made:

1. The diameter of the fiber was equal to the diameter of the Ni nanoparticle. As a consequence of low electron doses, fast-moving particles, and an integration time of at least 1 second, Ni nanoparticles looked blurry making their exact diameter hard to determine accurately. It is generally accepted that Ni particle and fiber diameters match [5, 18].
2. CNFs had the 3D shape of a hollow cylinder.
3. The diameter of the fiber did not change significantly throughout the length of the fiber.
4. CNFs did not grow in the z-axis.

The amount of carbon grown per second at a specific time (t) was determined by (2.7). The CNF growth rate at a specific time (t) was determined by (2.8). Where ρ_c (2.267 g mL^{-1}) and ρ_{Ni} (8.902 g mL^{-1}) are the respective densities of carbon and nickel, and ΔL the length (nm) of the grown CNF in Δt amount of time (s). The radii were determined using the intensity profile in ImageJ (Figure 2.1B). Because these profiles were generally quite rough, making determining radii more difficult, they were smoothed using (2.9). The extreme points of this smoothed profile resulted in r_{outer} and r_{inner}.

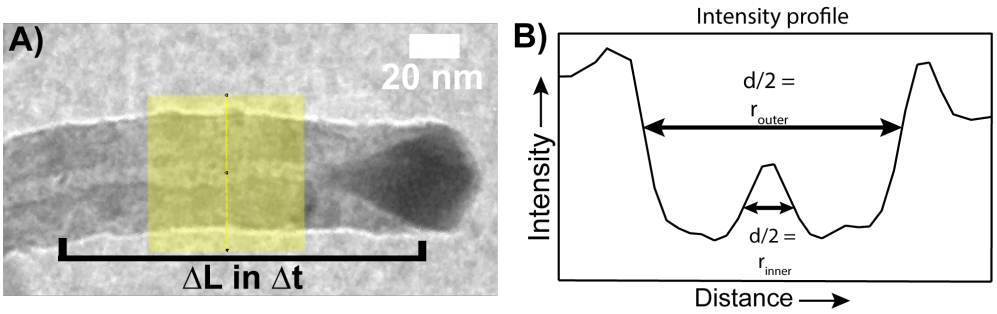

Figure 2.1: Schematic overview of CNF measurement. (A) The length (ΔL)of a CNF was measured over a period of time (Δt). Using a line scan in ImageJ, an intensity profile (B) was plotted. The inner ($r_{\mathbf{inner}}$) and outer ($r_{\mathbf{outer}}$) diameters of the fiber were determined using the extreme points of this profile.

$$C(\mathrm{nm^3 s^{-1}}) = \frac{\pi * (r_{\mathrm{outer}}^2 - r_{\mathrm{inner}}^2) * \Delta L}{\Delta t} \tag{2.7}$$

$$\text{Carbon growth rate } (\frac{C(\mathrm{g})}{Ni(\mathrm{g})}\mathrm{min^{-1}}) = \frac{C(\mathrm{nm^3 s^{-1}}) * \rho_C/60}{4/3 * \pi * (r_{\mathrm{outer}}^3) * \rho_{Ni}} = r_{\text{growth rate}} \tag{2.8}$$

$$y_n = 0.7 * x_n + 0.3 * y_{n-1}, \text{ for n} \geq 2 \qquad y_1 = x_1, \text{ for n} = 1 \tag{2.9}$$

Applying (2.8) to an individual particle resulted in a list of carbon growth rates ($\mathrm{r_{growth\ rate}}$) at time t. To reduce human error during CNF measurements, these were then averaged every 3 data points according to (2.10), resulting in (r_i). Lists containing (r_i) were then sorted according to their respective Ni particle size and time (t). These were then averaged using (2.11), resulting in an average growth rate for a specific particle size (μ_{size}) at time t. The standard deviation (σ_{size}) within these carbon growth rates (r_i) was determined using (2.12). μ_{size} combined with σ_{size} plotted at their respective t resulted in Figure 3.6 and Figure 3.7.

$$r_i = \frac{r_{\text{growth rate}}[i] + r_{\text{growth rate}}[i+1] + r_{\text{growth rate}}[i+2]}{3} \tag{2.10}$$

$$\mu_{\mathrm{size}} = \frac{1}{N}\sum_{i=1}^{N} r_i \tag{2.11}$$

$$\sigma_{\mathrm{size}} = \sqrt{\left(\frac{1}{N-1}\right)\sum_{i=1}^{N}(r_i - \mu_{\mathrm{size}})^2} \tag{2.12}$$

2.5.2 Weighted growth rate deviation

In order to compare the carbon growth rate deviation of individual particles between supports, the growth rate standard deviation of individual particles was determined using (2.14) and divided by their average growth rate (2.13) to result in (2.15). Particles were selected which had a minimum of 9 data points ($\mathrm{r_{growth\ rate}}$) with a value of > 0.

$$\mu_{\mathrm{particle}} = \frac{1}{N}\sum_{i=1}^{N} r_{\text{growth rate}} \tag{2.13}$$

$$\sigma_{\text{particle}} = \sqrt{\left(\frac{1}{N-1}\right)\sum_{i=1}^{N}(r_{\text{growth rate}} - \mu_{\text{particle}})^2} \tag{2.14}$$

$$\text{Weighted growth rate deviation} = \sigma_{\text{particle}}/\mu_{\text{particle}} \tag{2.15}$$

2.5.3 Surface activity

The surface activities of particles in Figure S5.15 were determined by (2.16). This was done by dividing (2.7) by the surface area of the particle with radius r_{outer}. It was assumed that the particle and fiber diameters were equal [5].

$$\text{Surface activity } ((\text{nm}_{\text{C}}^3\ \text{s}^{-1})\ /\ (\text{nm}_{\text{Ni}}^2)) = \frac{C(\text{nm}^3\text{s}^{-1})}{4 * \pi * r_{\text{outer}}^2} \tag{2.16}$$

2.5.4 Growth factor

In order to visualise the periods of time a particle was showing no growth, growth factors (f_{g}) were calculated according to (2.17). A particle was selected for analysis if it fulfilled the following conditions:

1. It continued growing carbon after it was (temporarily) showing no growth.
2. It was in-frame for the entire image series.
3. It was growing carbon for the entire image series, neglecting condition (1).

A schematic overview is presented in Figure 2.2.

$$f_g = \frac{\#\text{ frames showing growth}}{\#\text{ total frames}} \tag{2.17}$$

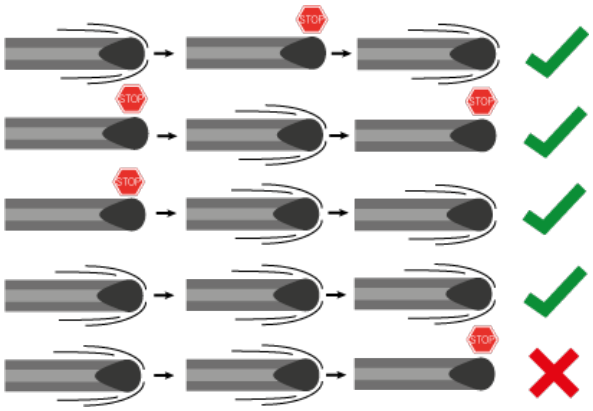

Figure 2.2: Visual representation of conditions set during f_{g} analysis.

2.5.5 Average particle shape

In order to get an average Ni nanoparticle shape, images were acquired of the same particle. The particle had to be active and in focus the entire time and could not grow visibly in the z-axis, as this would significantly influence results. A total of 10 images were taken of a single particle every 5 frames. Using PhotoshopCS6 (Adobe Inc.) [57], the frames were orientated in the same direction and stacked on top of each other. In order to average out all images, the opacity of an image was adjusted according to (2.18), where n is the layer number of the frame. The Ni nanoparticle ratio of the acquired image stack was then determined using the intensity profile in ImageJv1.54, according to (2.19). Where length is the distance alongside and height is the distance perpendicular to the fiber.

$$\text{Opacity} = \frac{100}{n} \tag{2.18}$$

$$\text{Particle ratio} = \frac{\text{Length}}{\text{Height}} \tag{2.19}$$

Chapter 3

Results & discussion

3.1 Catalyst characterisation

3.1.1 Support characterisation

Using physisorption and titration, the structural properties of supports were determined and are presented in Table 3.1. Due to the hygroscopic character of MgO, it was not possible to determine the surface group density using potentiometric titration, as the addition of 0.1 M HCl to $Mg(OH)_2$ likely formed magnesium chloride. The liquid phase oxidation treatment of GNP resulted in a loss of surface area and pore volume. However, the density of acidic surface groups had significantly increased compared to pristine GNP, resulting in a lowered PZC. Together with a total yield of approximately 87% indicating a loss of carbon, the structure of GNP-ox might be weakened compared to GNP. SiO_2 and TiO_2 showed lowered pore volume and surface areas compared to the carbon supports, which may result in larger particles as there is less surface to distribute precursors. TiO_2 has a higher surface group density compared to SiO_2, which might result in better particle dispersion and stronger metal-support interaction. All support materials do not possess a well-defined porous structure as they consist of random stacked graphene layers (GNP/GNP-ox) or agglomerates (SiO_2/TiO_2). Nevertheless, similar mesoporous structures are present in these, which should allow for proper capillary action 5.3. MgO shows smaller pore sizes compared to other support materials, as these pores mainly arise from interparticle distances.

Powder X-ray diffraction (XRD) gives us information regarding the crystal phases present in the support materials. In Figure S5.1 the diffractograms are represented. From these, it can be concluded that SiO_2

Table 3.1: Properties of unimpregnated supports: (a) The density of acidic surface groups per gram of support material was determined using potentiometric titration. (b) Point of zero charge of bare supports was determined using mass titration. (c) BET surface area and pore volume (p/p^0=0.995) determined using N_2-physisorption.

Support	Acidic groups (#groups nm^{-2})^a	PZC^b	BET surface area (m^2 g^{-1})^c	Pore volume (cm^3 g^{-1})^c
GNP-500 (oxidized)	0.45	2.1	418.45	0.69
GNP-500	0.09	3.5	510.13	0.73
SiO_2 (aerosil380)	0.03	4.0	324.83	0.73
TiO_2 (p90)	0.29	5.2	82.75	0.49
MgO (powder)	NaN	11.7	156.56	0.27

Table 3.2: Overview of synthesised Ni catalysts using incipient wetness impregnation. Crystallite sizes (TEM and XRD) were determined from passivated catalysts after reduction.

Support	Ni weight loading (wt.%)	Heat treatment (°C) (+ flow)	Reduction temperature (°C)	Ni crystal size TEM (nm)	Ni crystal size XRD (nm)
Ni/GNP-ox	23.0	300 (N_2)	350	11.9 ± 10.0	21.4
Ni/GNP	25.8	300 (N_2)	350	8.9 ± 3.7	7.0
Ni/SiO_2	15.3	500 (1:20 NO:N_2)	450	10.6 ± 3.8	8.2
Ni/TiO_2	9.3	450 (1:20 NO:N_2)	550	14.0 ± 4.75	9.3
Ni/MgO	-	350 (1:20 NO:N_2)	550	NaN	NaN

(aerosil380) is an amorphous support, evidenced by a broad diffraction peak between $2\theta = 17 - 35°$. GNP and GNP-ox have characteristic diffraction peaks at 2θ = 30, 52, 64° due to the presence of the graphitic phase. TiO_2 (p90) consists of an anatase and rutile phase mixture. Using the Spurr-Meyers equation [58], it was estimated that the mixed phase consists of approximately 86% anatase and 14% rutile. Even though rutile is thermodynamically more stable compared to metastable anatase, a phase transformation will likely not occur at the temperatures used in our experiments [59].

3.1.2 Synthesised catalyst characterisation

Ni was deposited on all support materials using incipient wetness impregnation. A general overview of the preparation conditions and particle sizes of the different catalysts are presented in Table 3.2. Earlier experiments in our group showed that Ni particles < 7 nm hardly grow CNFs. Therefore we aimed to synthesise particles in a 9-15 nm size range. The goal was to be as close to this lower limit, as larger particles typically do show growth, most likely because of a better balance between carbon supply and CNF nucleation.
Ni particles within this range were successfully synthesised on all support materials with the exception of Ni/MgO. This catalyst is separately discussed in subsection 3.1.3. In the case of GNP and GNP-ox, a single impregnation method resulted in Ni particles below this 8 nm lower limit. Therefore a double impregnation method was used in order to increase the weight loadings and thus the average Ni particle sizes (Figure S5.6). Their representative TEM images are shown in Figure 3.1 A-B. Generally, Ni particles were well dispersed over the supports surfaces. The double impregnation approach for Ni/GNP resulted in relatively low polydisperse particle size compared to Ni/GNP-ox. Some large Ni particles are present on GNP-ox due to agglomeration, resulting in a high particle size dispersity. Normally this is an undesired effect, however, during in-situ TEM we can measure individual particles with different sizes which are then 'filtered' out on their size. This makes the particle range during size effect studies broader.

In contrast to the carbon supports, the impregnation of SiO_2 and TiO_2 resulted in Ni particles above the aimed size range. Lowering weight loadings would result in smaller particles and thus a lower nanoparticle density (see Table S5.1). However, as a consequence fewer Ni particles would be present in-frame during in-situ TEM experiments, making comparisons more difficult and statistically less relevant. To maintain a high particle density, 5% NO in N_2 was added during the heat treatment of Ni/SiO_2 and Ni/TiO_2 to allow a more gradual decomposition resulting in reduced nanoparticle sizes. As higher temperatures during the heat treatment of Ni/TiO_2 can stimulate the formation of $NiTiO_3$ species [60], temperatures were kept at 400 °C during synthesis. As seen in Figure 3.1 C-D, this resulted in a relatively good dispersion of Ni particles over the support surface. However, in TEM, the contrast difference between Ni particles supported on SiO_2

and TiO_2 is quite low due to higher atomic values of the oxide support compared to carbon supports. This makes CNF growth observations, especially during low-resolution in-situ TEM experiments, more difficult.

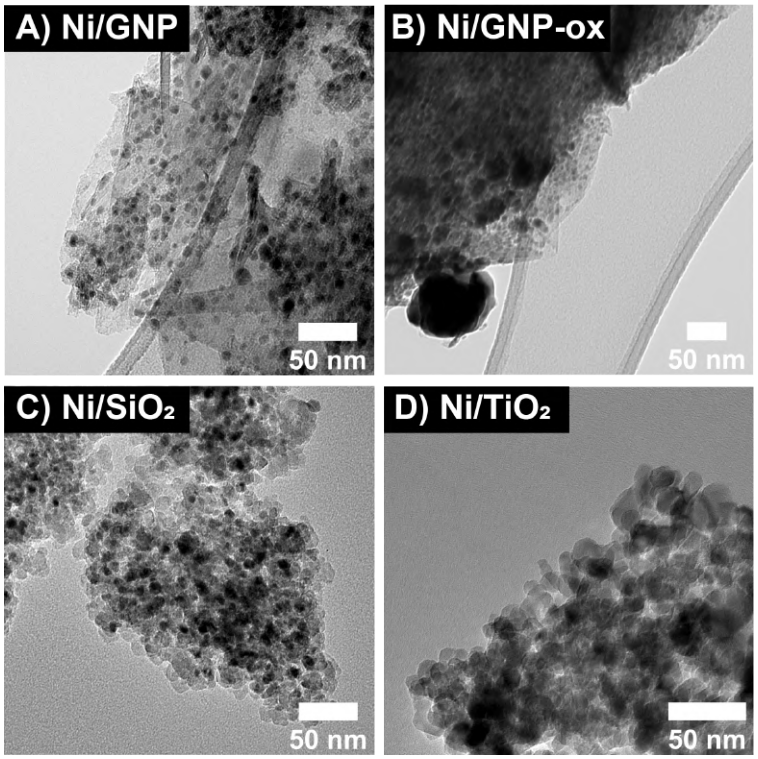

Figure 3.1: Transmission electron microscopy images of synthesised catalysts A) Ni/GNP B) Ni/GNP-ox C) Ni/SiO_2 and D) Ni/TiO_2. Samples were reduced and passivated, before being transferred to a carbon coated copper TEM grid via ambient air.

The reduction temperatures were determined using temperature-programmed reduction (TPR). The normalised reduction profiles of NiO supported on the different materials are shown in Figure 3.2 A. Only the single impregnated NiO/GNP and NiO/GNP-ox samples are shown, as the double impregnated samples resulted in too little product for TPR measurements. Nevertheless, the carbon-supported catalysts show hydrogen uptake above 380 °C , which is due to carbon support methanation by Ni particles. Therefore, to avoid severe support methanation during the reduction step, Ni/GNP and Ni/GNP-ox samples were reduced at 350 °C. The reduction profile areas of NiO species were the same between different supports, with the exception of Ni/GNP-ox which has a larger amount of H_2 adsorped. This is likely explained by the loss of support material during heat treatment and oxidation step, increasing the relative weight loading of NiO. As acidic surface groups on GNP(-ox) decompose from 100 °C upwards, the higher loss on Ni/GNP-ox compared to Ni/GNP is due to an increase in surface group density [38].

Supported Ni catalysts show two reduction peaks. Around 270 °C is assigned to reducing bulk NiO weakly interacting with the support. The higher peak is due to the strongly interacting NiO with the support material. Compared to other supports, Ni/TiO_2 has a relatively low amount of weakly interacting NiO species, resulting in a weak shoulder band around 270 °C. The largest amount of NiO strongly interacts with the support material via $NiO\text{-}TiO_2$ species [60]. This might indicate strong wetting of the particles on the support surface or small particles. However, the latter would be in contrast to observed crystalline sizes. When looking at stronger interacting NiO, these species are reduced around 350 °C at TiO_2/GNP/GNP-ox with

no clear differences, whereas it is reduced around 470 °C on SiO_2. This indicates a stronger metal-support interaction for silica-based catalysts, due to NiO-SiO_2 species. However, Ni/TiO_2 showed H_2 uptake around 520 °C due to the reduction of NiTiO3, see Figure S5.5 [60]. This SMSI is unwanted as can diffuse over the Ni particle surface, deactivating active metal sites. Therefore Ni/TiO_2 samples were reduced at 550 °C.
The different reduction temperatures may result in different extents of reduction between catalysts, which can introduce differences in catalytic activity. It is unknown how significant this effect is, as the catalysts are reduced twice (ex-situ and in-situ), despite the catalyst's passivation in between reoxidising the top layer. Still, varying the reduction temperature did not seem to affect the carbon growth rate (see Figure S5.8), nevertheless, more extensive investigation might be deemed necessary.

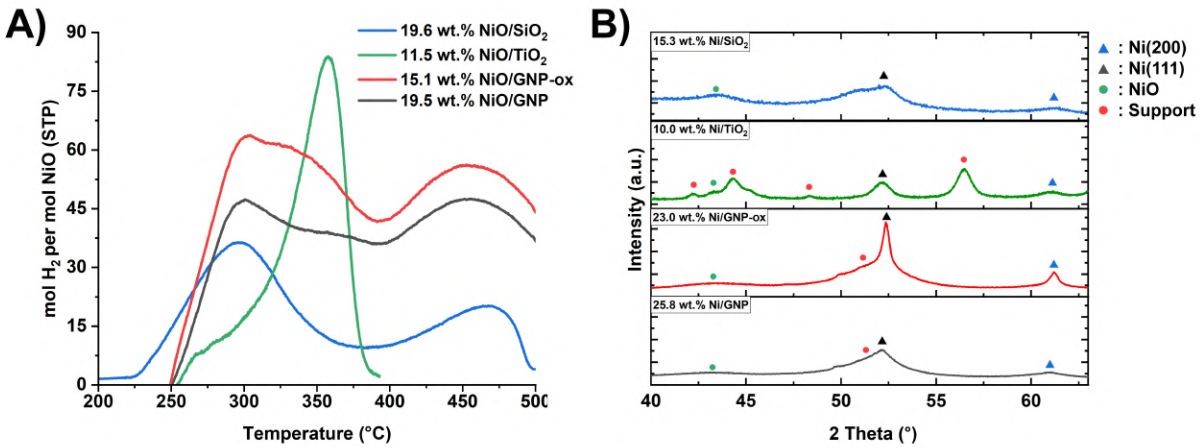

Figure 3.2: A) Temperature-programmed reduction profiles of NiO supported on different materials after heat treatment. An oxidation treatment was performed prior the measurement to ensure full oxidation of NiO. Temperature program: 30-500 °C, 3 °C min, 5% H_2/Ar (40 mL min^{-1}). B) Powder X-ray diffraction patterns of prepared catalysts. Samples were passivated in air after reduction, oxidising the top metal layer.

Powder X-ray diffraction (XRD) was used to characterise the present crystallite phases in the catalysts, see Figure 3.2. In all catalysts the Ni (111) and Ni (200) diffraction peaks at 2θ = 52 and 61° are present in the same ratio, meaning Ni crystals are formed during reduction. Still, NiO diffraction peaks are present at 43° due to the passivation of the sample in air, reoxidizing the top layer. These NiO species should not be present during the in-situ TEM experiment, as samples are in-situ reduced prior to the experiment. The sharp peaks in the Ni/GNP-ox diffractogram are a consequence of the formation of large Ni-particles due to agglomeration. The lack of Ni phyllosilicates (2θ = 40-44°) and $NiTiO_3$ (2θ = 58°) diffractions indicate an absence of SMSI [55, 60]. However, these interactions may also be finely dispersed, in which case it is difficult to detect in XRD.

3.1.3 Preliminary results Ni/MgO catalysts

Magnesia powder was impregnated with a 4 M $Ni(NO_3)_2$ in water and a 1 M $Ni(NO_3)_2$ in ethanol precursor. The latter was done as to avoid the formation of $Mg(OH)_2$ species in aqueous solutions. Still due to the hydrated precursor, an EtOH: H_2O phase was formed and prone to $Mg(OH)_2$ formation. The 1 M $Ni(NO_3)_2$ in ethanol precursor resulted in a fine homogeneous colour distribution over the support observed by eye. This was in contrast to the 4 M $Ni(NO_3)_2$ precursor which resulted in an uneven colour distribution. This was possibly a consequence of the formation of $Mg(OH)_2$ and dissolving Mg^{2+} in the acid precursor solution. Therefore the absence of water is essential for fine precursor distribution on MgO. Further catalyst preparations and analysis were performed with the 1 M $Ni(NO_3)_2$ precursor in 9:1 EtOH: H_2O. This resulted in

a low weight loading (4.6 wt%. Ni/MgO), which is undesired for in-situ TEM studies. However, a different synthesis approach would be needed to increase this.

Impregnated MgO-based catalysts underwent a heat and reduction treatment (see Table 3.2). Heat treatment temperatures were kept at 350 °C, as higher temperatures may stimulate Ni^{2+} diffusion in the MgO support, forming a solid NiO-MgO solution [61]. The TPR profile of the oxidised NiO/MgO sample in Figure 3.3 A shows 2 major hydrogen uptake peaks. This indicates the presence of NiO, as these peaks are not visible in the MgO TPR profile. The lower peak is assigned to reducing bulk NiO and the higher peak to strong interacting NiO with the MgO support. The ramp of the baseline is assigned to the slow uptake of H_2 by the MgO. The amount of H_2 adsorbed did not differ too significantly from the other prepared catalysts, meaning large amounts of NiO are reduced. A weak peak can be seen around 500 °C, indicating the presence small amount of stronger interacting NiO, perhaps due to NiO-MgO solid solutions [61].
NiO and Ni diffraction peaks are not present in the XRD diffractogram, see Figure 3.3 B. Differences between NiO and MgO diffraction peaks are indistinguishable as they overlap throughout the diffractogram. The absence of Ni peaks in the Ni/MgO diffractogram indicates the absence of large Ni crystals on the surface or the formation of amorphous structures. This is in line with the observations of Takenaka *et al.*, who likewise had a high Ni dispersion over the MgO support using the IWI method [35]. This indicates possible migration of the Ni^{2+} species into the MgO support, preventing the formation of large Ni crystals [61].

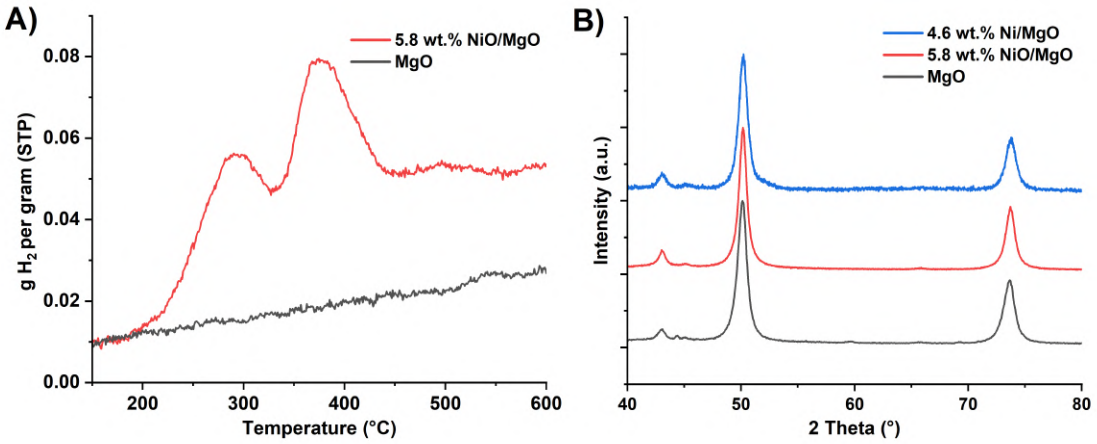

Figure 3.3: A) Temperature-programmed reduction profiles of NiO supported on MgO and as received MgO. An oxidation treatment was performed prior to the NiO/MgO measurement to ensure full oxidation. Temperature program: 30-800 °C, 3 °C min, 5% H_2/Ar (40 mL min^{-1}) B) Powder X-ray diffraction patterns of different phases of Ni on MgO. Ni/MgO was measured using a dome to ensure no oxidation.

In Figure 3.4 representative TEM images are shown of the passivated Ni/MgO catalyst. It is hard to differentiate Ni particles from the cloud-like MgO support due to low mass-thickness-contrast. Nevertheless, some metallic Ni particles are distinguishable, as relatively few are present with high polydispersity. This varies depending on the imaged catalyst particle. The impregnation has affected the structure of the MgO, as more rugged structures are present. This might be of origin to an amorphous structure due to the formation of NiO-MgO solid solutions or amorphous NiO layers over the MgO surface [62]. As a result of the absence of enough Ni particles in the ideal nanoparticle size range, it was decided to not perform in-situ TEM experiments with the Ni/MgO sample.

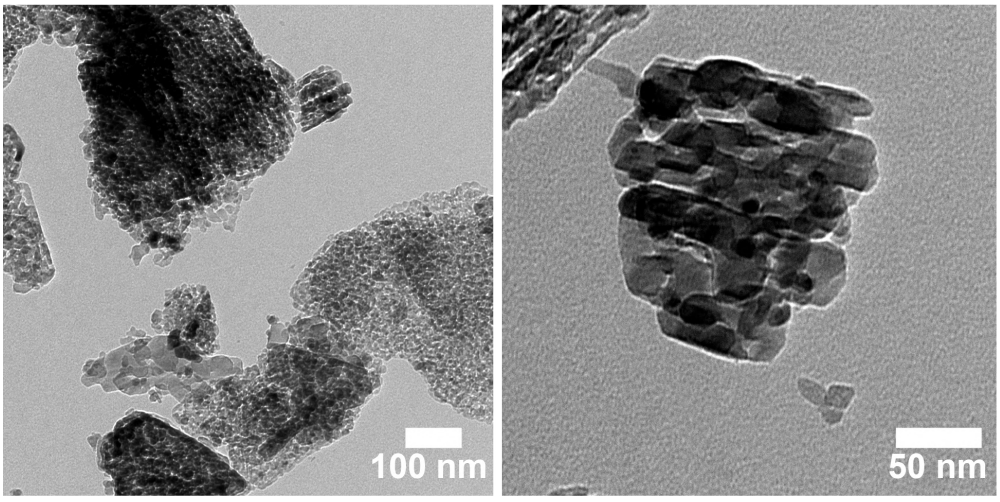

Figure 3.4: 5 wt.% Ni/MgO catalysts prepared using a 1 M $Ni(NO_3)_2$ precursor in 9:1 EtOH:H_2O. The sample was passivated in ambient air after reduction.

3.2 In-situ TEM experiments

In-situ TEM experiments were performed with Ni particles supported on GNP/GNP-ox/SiO_2/TiO_2. In this section, we discuss the CNF formation and several observations made during these experiments. The volume of the CNFs that were grown by individual particles was measured from the obtained image series. The carbon growth rate is reported in units of C (g) / Ni (g) min^{-1} according to (2.8).

However, before we start, it is important to be aware of several factors which might influence the presented carbon growth rate.

1. We are making 3D assumptions from 2D projections, thus not accounting for growth in the z-axis. In other words, we assume everything grows directly in the $x-y$ plane. This will always result in growth rate deviations. For example, when a fiber temporarily travels at an angle of 45 ° to the x-axis, which sometimes is hard to distinguish, 70% of the actual fiber length is measured. This assumption is the biggest contributor to carbon growth rate deviations.

2. Experiments were performed at fairly low signal-to-noise ratios. As a consequence, it is hard to code a tracking program that can reliably track a fiber over time. This is especially the case during crowding, the process where multiple fibers overlap each other, making the fibers difficult to distinguish. Therefore fibers are measured by hand, introducing human error. As we measure a dozen of frames per fiber, we hope to average out this error.

3. There is a first come, first served scenario. What we mean by this is that the first particles observable are the most active, whereas slower particles may be completely covered by crowding and less visible. This may introduce some bias in growth rate comparisons as particles with an above-average carbon growth rate may be overrepresented in some measurements.

3.2.1 Catalytic tests: Particle size dependency

In-situ TEM experiments resulted in CNFs being grown on all catalysts. A representative experiment is shown in Figure 3.5. Multiple images series were made per catalyst and QR codes/hyperlinks to the videos can be seen in the appendix 5 A2. Upon exposing the catalysts to 3:1 CH_4:H_2, fibers up to tens of microns long were grown during experiments. Particles as small as 7 nm up to 80 nm were able to facilitate fiber

nucleation. Depending on the activity and the amount of fibers in the frame, the camera was shifted away from the busy area in order to image active fibers. Not all particles nucleated fibers, especially particles ≤ 7 nm were never observed to grow CNFs. These particles may eventually nucleate CNFs, as they reach a sufficient size due to sintering or Ostwald ripening. We were only able to observe these phenomena on GNP/GNP-ox due to high z-contrast, however, Ni particle sintering at high temperatures is not uncommon on SiO_2 and TiO_2 [63, 64]. This sintering resulted in the observation of larger crystallite sizes compared to those mentioned in Table 3.2. Individual particles deactivated as carbon accumulated at the active sites, eventually encapsulating the particle (Figure S5.16). Encapsulated particles could eventually collide with other Ni particles agglomerating to form a larger Ni crystal. In this case, particles could continue to grow CNFs (Figure S5.17). In another method of deactivation, particles stopped growing fibers due to entanglement. This was a consequence of slowly reducing growth space.

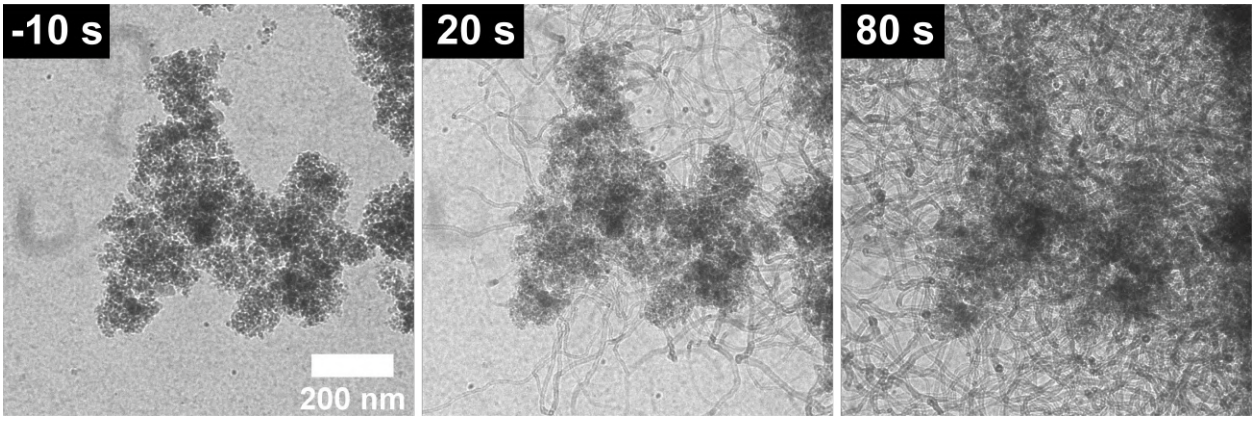

Figure 3.5: In-situ TEM experiment of Ni/SiO_2 exposed to 3:1 CH_4:H_2, 1 bar, 0.1 sccm at 550 °C. Electron doses of 13 e^- $Å^{-2}$ s^{-1}. The sample was under vacuum (t = -10 s) before the reaction atmosphere was introduced at $t = 0$ s. As time progresses, CNFs continue to grow and obstruct the field of view.

The obtained image series were analysed by measuring the CNF growth of individual particles over time. Different particles at various timestamps are grouped together by size and their average carbon growth rate plotted was in Figure 3.6. What is seen here are particles that fulfilled the criteria set in section 2.5.1. Therefore it does not account for particles that are deactivated or inactive. As a consequence of CNF crowding and low z-contrast between the support and Ni particles, especially for the Ni/SiO_2 and Ni/TiO_2 catalysts, quantitative estimates of inactive particles are difficult to make during in-situ TEM experiments. Furthermore, we mentioned a first come first serve scenario and measured particles are likely the most active. As a result of these factors, the measured growth rates are not completely representative of the bulk catalyst carbon growth rates. Regarding Figure 3.6, it is important to remind one that these measured particles are visible in the frame. As a small part of the catalyst is imaged, not all particle sizes might be present in the field of view. Also as the whole system is expanding, probabilities are lower for CNFs to grow in focus. Missing data points do therefore mean that they are not observed, however, this is still a slight indication that they are inactive (Figure 3.7 A). It should be noticed that comparing the presented standard deviations in carbon growth rate between particle sizes and catalysts might be misleading. Data points consist of various amounts of particles that are measured over different durations of time, making comparisons in terms of standard deviation unfair. These differences will be discussed separately later.
Looking at Figure 3.6, carbon growth rates decrease over time as carbon is accumulated on the active metal sites. Also the initial carbon growth rate tends to be the highest on smaller particles. There is no clear trend indicating that the surfaces of smaller particles are more active in decomposing methane (Figure S5.15). This is caused by particles growing CNFs (> 7 nm) already operating in a size range, where traditional particle size effects like extra step edges and surface defects do not play a significant role [30]. Therefore the

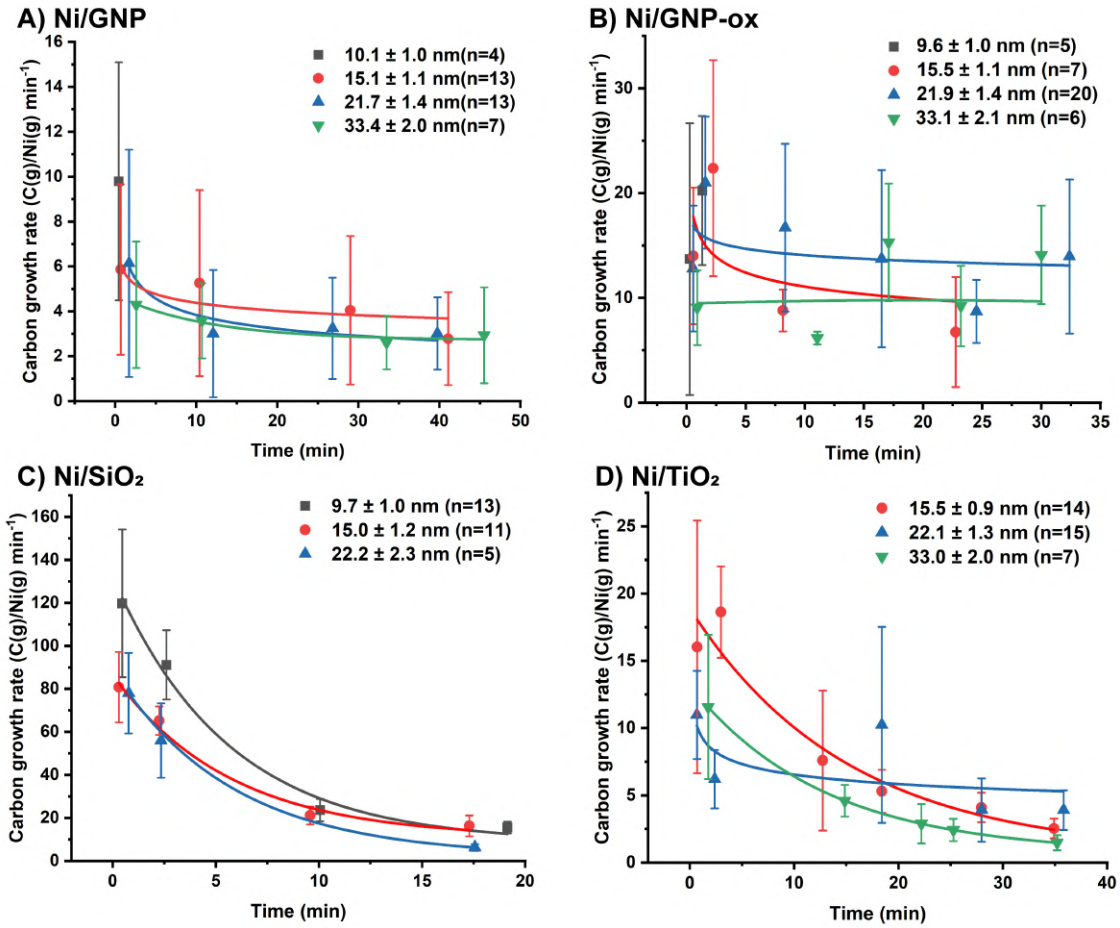

Figure 3.6: Carbon growth rates analysed from in-situ TEM image series according to 2.5.1. The measured growth rates of individual particles are averaged every 3 timestamps. Each data point is an average of multiple of these active particles and the growth rate deviations within these particles. Exponential decay functions are fitted. n is the total population of particles over all different data points. All experiments were performed at 550 °C, 1:3 H_2:CH_4, 1 bar, 0.1 sccm. Electron intensities were A) 10 B) 10 C) 13 and D) 10 e^- $Å^{-2}$ s^{-1}

larger surface-to-volume ratio is the main contributor to higher carbon growth rates, as less Ni is necessary per active surface area. Please note that particles behave liquid-like during CNF formation. Active sites emerge and disappear as a result of forming new graphene layers, complicating statements regarding exposed crystal fates [19]. Growth rate deviations are the largest at the beginning of the experiments. This is due to these data points containing the largest number of particles and the fastest deactivation rate. The latter is logical as this phase has the highest number of active sites, resulting in more significant amounts of carbon processed and thus a higher chance of active site blockage.

Deactivation rates of particles supported on Ni/GNP and Ni/GNP-ox were size dependent, as seen in Figure 3.6 A-B. Deactivation rates of particles $>$ 10 nm were high, as no active particles were observed after a few minutes of growth. These particles have a too high carbon supply compared to the ability of carbon atoms to diffuse away and nucleate fibers. This results in a loss of active surface area and quick encapsulation. Upon increasing size, deactivation seems to be less evident on these catalysts. For example, Ni/GNP-ox has particles with a 15 nm size average particles deactivate relatively quickly over time, whereas

larger particles deactivate slowly. Particles with an average size of 33 nm showed no distinct decrease in growth rate. The reduced surface area and larger Ni volume thus result in a fast carbon diffusion from the active sites and thus low deactivation rates as particle size increases. Still, it should be noticed that trends are difficult to fit due to large standard deviations in the growth rate. Regarding the optimal particle size for Ni/GNP and Ni/GNP-ox, the highest initial carbon growth rates are acquired at small sizes ($\sim$ 10 nm). However, as these deactivate quickly larger particles ($\sim$ 33 nm) seem to have the best long-term performance.

When comparing particles on Ni/SiO_2 and Ni/TiO_2 in Figure 3.6 C-D, the deactivation rates are not distinguishable dependent on their size. The carbon growth rates exponentially decrease over time as surface sites get encapsulated. One could argue that smaller particles have a steeper deactivation curve. This would make sense as these have a relatively larger amount of methane decomposed due to a higher surface-to-volume ratio. Nevertheless, if you account for the standard deviation there are no distinct differences in their deactivation rate. This means that there is no significant particle size effect regarding the transfer of deposited carbon from the surface to the CNF. Ni particles with a size average of 22 nm supported on TiO_2 (Figure 3.6 D) differ from this trend, several factors may be of influence. First, it may highlight an analysis error in these types of experiments. Only a few particles are measured at a random location on a small part of the catalyst, which results in low statistical trustworthiness. Particles that over-/underperform can contribute significantly to the resulting plot, resulting in deviations from the general trend which might not be representative of the general performance of that specific particle size. Second, the measurement of around 18 minutes is a significant outlier, which is supported by the large error bar. This influences the fit disproportionally. Third, variations in carbon growth rate can originate from the mixture of the anatase and rutile phases in TiO_2. CNFs may be deposited differently depending on the crystal phase on which the Ni particle is located. In the case of Co/TiO_2 catalysts during Fischer-Tropsch catalysis, anatase planes were prone to a more extensive SMSI coverage compared to rutile, deactivating active metal sites [65]. Shah *et al.* found that the anatase- rutile ratio influences the CNF yield in Co/TiO_2 catalysts [66]. Therefore the possible influence of the phase mixture in Ni/TiO_2 catalysts should not be excluded. However, during in-situ TEM experiments, it is hard to differentiate these as it is difficult to track the origin of the fibers, especially when these arise from the bulk of the material. The lack of resolution and a low rutile percentage (14%) also make it unhelpful to distinguish between them.

Smaller Ni particles on the oxide supports seemed to be preferred, however, we do not know if this lack of particle size dependency on the deactivation rate is sustained outside this size range. Especially when one considers that Takenaka *et al.* determined the optimal Ni particle size on SiO_2 to be around 60-100 nm [33]. Still, the optimal Ni particle size regarding activity and deactivation seems to be dependent on the support material used.

3.2.2 Catalytic tests: Support comparison

In order to compare carbon growth and deactivation rates, similar-sized particles on all supports are plotted against each other as a function of time in Figure 3.7. The raw data is the same as in Figure 3.6. The data points for 9-10 nm on Ni/TiO_2 and 33 nm on Ni/SiO_2 are missing, as not enough particles were present in the field of view for analysis. Therefore it does not necessarily mean these are not active. The order in the initial activity is $Ni/SiO_2 >> Ni/GNP\text{-}ox \approx Ni/TiO_2 > Ni/GNP$. It is important to note that Ni/SiO_2 is performed under slightly higher electron doses (13 compared to 10 e^- $Å^{-2}$ s^{-1} in other experiments), possibly promoting methane decomposition. Still, it is unexpected that this increase influences the carbon growth rate significantly. As seen in Figure 3.7, the high carbon growth rate of Ni/SiO_2 also results in the fastest initial deactivation rate, as larger amounts of deposited carbon will result in more accumulation at active sites. As a consequence, the carbon growth rate is similar to other supports after 10-15 minutes of growth. Due to the length of the Ni/SiO_2 experiment, it is difficult to state how this deactivation compares over longer periods of time. Furthermore, the difference in particle size dependency between the carbon and oxide supports can be clearly seen. The deactivation of 9-10 nm particles on carbon supports was drastic, whereas particles on SiO_2 grew CNFs for tens of minutes. Upon increasing size, the deactivation rates of

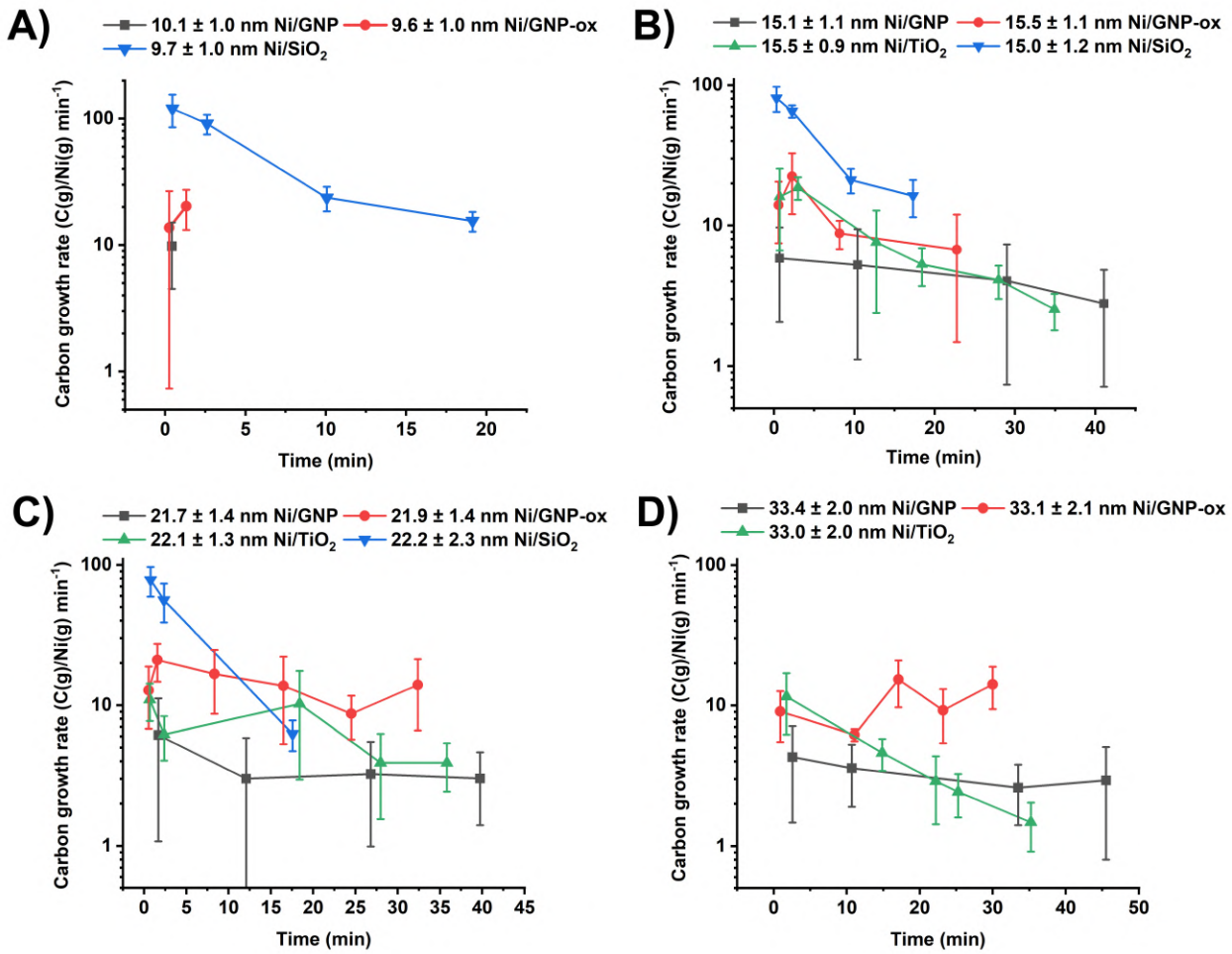

Figure 3.7: Growth rate comparisons of similar-sized particles on different supports as a function of time. The measured carbon growth rates of particles are averaged every 3 seconds. Each data point is an average of multiple active particles and the growth rate deviations within these particles. All experiments were performed at 550 °C, 1:3 H_2:CH_4, 0.1 sccm, 1 bar.

particles on oxide supports showed to be higher compared to the carbon supports. Interestingly, differences in carbon growth rates are present when minutes have passed and long CNFs are grown. It was already stated unlikely that at these particle sizes the metal-support interactions would have any direct kinetic effect on the decomposition of methane [41], particularly when CNFs have grown in between. Therefore the nucleation phase of CNFs greatly influences the activity of particles over time.

When directly comparing the oxide supports, Ni/SiO_2 had a significantly higher initial activity compared to Ni/TiO_2, which had a similar deactivation curve. Upon introducing methane, the first CNF growth was observed on Ni/SiO_2 and Ni/TiO_2 after $\sim$ 4 and $\sim$ 8 seconds respectively. Therefore carbon diffuses more quickly to the metal-support interface on Ni/SiO_2 compared to Ni/TiO_2.
Most Ni particles on TiO_2 grew CNFs according to the tip-growth mechanism, nevertheless, multiple particles nucleated CNFs according to the base-growth mechanism, see Figure 3.8. The CNF grew on top of the Ni particle, which was stretched while still being connected to the TiO_2 support. When space got limited for the CNF to grow, the fiber was orientated proportionately to the Ni-TiO_2 interface. At this point, the

consequent pressure built up from carbon was enough to separate the Ni particle from the support, resulting in tip growth of CNFs. As this was not observed during Ni/SiO_2 experiments, this indicates strong metal-support interactions on Ni/TiO_2. The strong MSI would not necessarily result in base-growth, as some of Ni particles supported on TiO_2 appeared to remain inactive However, accurate quantitative estimations are challenging to make due to the low contrast. A higher surface group density on TiO_2 compared to SiO_2 results in a stronger interaction with the Ni particle and may inhibit its lifting from the support. Furthermore, hard-to-reduce SMSI ($NiTiO_3$) may prevent the particle from lifting from the support [23], but as these diffractions were not seen during XRD measurements, it is unsure to what extent these species are present.

If the MSI is stronger, the particle is held more strongly to the support surface during the CNF nucleation phase, and will result in a carbon concentration building up in the Ni particle at the metal-support interface. As a consequence, the Ni_3C concentration gradient flattens out inhibiting fast carbon diffusion from the active surface sites and eventually deactivation. As these sites are not suddenly reactivated, lower carbon growth rates are sustained throughout the CNF growth. This is in line with the findings of Li *et al.* who saw an increase in deactivation rate with increasing MSI, as this inhibits the lifting of the metal particle resulting in particle encapsulation [37]. Next to carbon accumulation, SMSIs species can also deactivate surface sites by migrating TiO_x ($x < 2$) species over the Ni surface[39], or by suppressing carbon diffusion through the bulk Ni which will also result in carbon accumulation [40]. This total reduction in active surface sites on Ni/TiO_2 particles lowers the carbon growth rate compared to Ni/SiO_2. Therefore stronger metal-support interactions negatively influence catalytic activity.

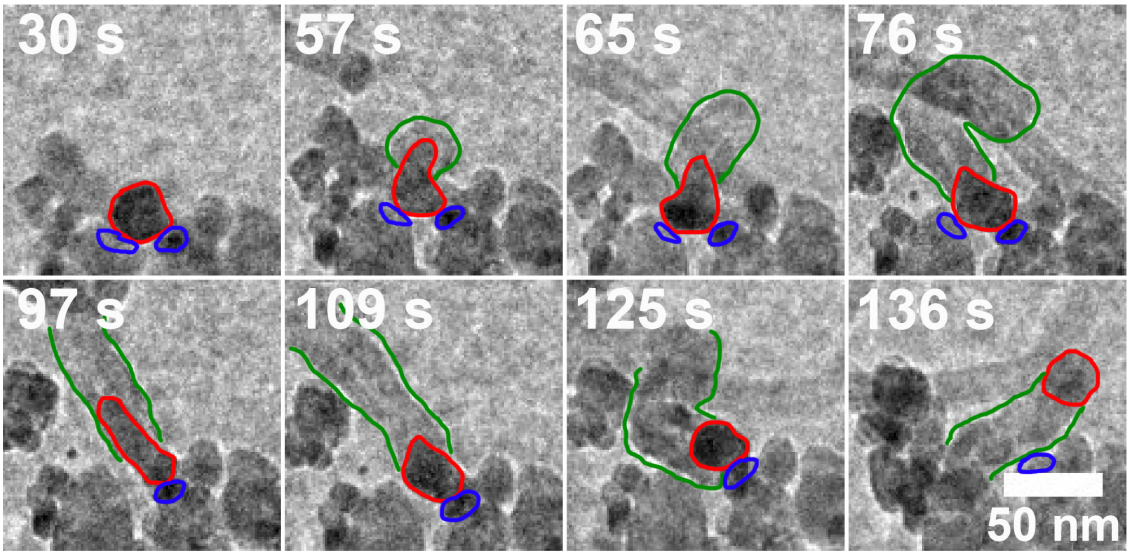

Figure 3.8: Base-growth followed up by tip-growth of a Ni particle supported on TiO_2. The Ni particle is highlighted in red and the nucleated CNF in green. The particle behaved liquid-like during base growth while still being connected to the TiO_2 contact patches highlighted in blue. Video can be seen in Figure S5.18. Reaction conditions are 550 °C, 1:3 H_2:CH_4, 1 bar, 0.1 sccm at 10 e^- $Å^{-2}$ s^{-1}

When comparing the carbon supports, both catalysts showed similar deactivation patterns with small particles deactivating quickly and larger particles showing steadier growth. Comparing the activity, Ni/GNP-ox had a 2-5 times higher carbon growth rate compared to Ni/GNP. When introducing methane during experiments, the first CNF growth was observed on Ni/GNP-ox and Ni/GNP after $\sim$ 4 and $\sim$ 8 seconds respectively. Therefore, carbon diffuses more easily and CNFs are nucleated faster on Ni/GNP-ox. The oxidation treatment of GNP resulted thus in a better performing catalyst, nevertheless comparisons based on the composition of the support surface are difficult to make.

One of the limitations of the in-situ TEM system is that in order to switch atmospheres the system, including the holder, has to be evacuated to approximately 4 mbar. After the in-situ reduction step during the in-situ TEM experiments of the Ni/GNP-ox catalysts, the holder was vacuum pumped in order to introduce the reaction atmosphere. When this reaction atmosphere was prepared in the external storage tank, the system was raised to 550 °C for catalytic experiments. However, in the supposed vacuum prior to the catalytic experiments, significant parts of the support were consumed as seen in Figure 3.9. Particles were observed to be consuming the support while behaving liquid-like, in which they may consequently split up into multiple particles or agglomerate. Possible electron beam effects are excluded as support consumption also took place outside the beam. This consumption was only slightly observable during Ni/GNP experiments compared to Ni/GNP-ox, meaning the liquid oxidation treatment weakened the GNP support by introducing multiple carbon defects. Likely, support methanation was the cause of this support consumption. During vacuum pumping of the system, a few mbar H_2 might be left in the holder from the in-situ reduction step. This proved to be enough to significantly consume the support at reaction temperatures. As the support consumption did not occur under 10% H_2 at atmospheric pressures, the thermodynamic equilibrium is shifted towards CH_4 formation at low pressures.

Support methanation introduces defect sites in the GNP-ox support. These defect sites can enhance the Ni binding energy [67], but may also provide a higher affinity for deposited carbon [16]. Additionally, defects can also introduce carbon into the Ni bulk, providing an extra carbon source [68]. These factors might provide a better base for CNFs to nucleate on, resulting in higher carbon growth rates. Nevertheless, comparisons between the catalysts are challenging to make. Initially, GNP-ox had a higher surface group density compared to GNP, however, these groups are mainly lost during the two heat and reduction treatments [38]. Combining this with the severe support consumption, the status of the GNP-ox surface is uncertain, making comparisons based on the carbon surface composition not feasible. Further investigations are thus necessary to investigate the structural properties of the GNP-ox and effect of support consumption on the catalytic performances.

When comparing the differences in carbon growth rate of the carbon to the oxide supports, possible explanations are less straightforward. One would expect the interaction of Ni with GNP to be less strong compared to Ni on TiO_2, due to the inert nature of GNP and lower amount of surface groups. Still, Ni/TiO_2 has a higher carbon growth rate. As the deactivation mechanisms differ between the metal oxide and carbon supports, this suggests other factors greatly influence the nucleation phase and therefore carbon growth rate. In the upcoming section, we identified two modes of CNF growth that might be of importance to this observation.

3.2.3 Catalytic tests: Continuous vs stuttering growth

During the catalytic in-situ TEM experiment, 2 growth modes were identified. A 'continuous growth' mode and a 'stuttering growth' mode as seen in Figure 3.10. In continuous growth, the Ni particles nucleate fibers consistently, without stopping, at consistent growth rates. Ni/SiO_2 and Ni/TiO_2 were both showing continuous growth (Figure 3.10 B). In stuttering growth, the Ni particles grow fibers inconsistently with large growth rate deviations (Figure 3.10 A). These particles may stop growing fibers before continuing with intermissions lasting seconds to minutes. This stuttering growth is often observed on the Ni/GNP and Ni/GNP-ox catalysts. It thus seems that during this growth, the amount of carbon input is not sufficient enough to sustain CNF growth.

Not much is discussed in the literature regarding these observations. 'Stuttering' growth occurs during the formation of bamboo-like CNFs, however, these structures do not seem to be present during the Ni/GNP and Ni/GNP-ox experiments [69, 70]. Furthermore, de Jong *et al.* discussed the saturation magnetisation of Ni-based catalysts at various timestamps during catalytic experiments and suggested that the steady growth occurs with either 'pulsed'-growth or a 'smooth'-growth [5]. However, no definitive answer is given regarding

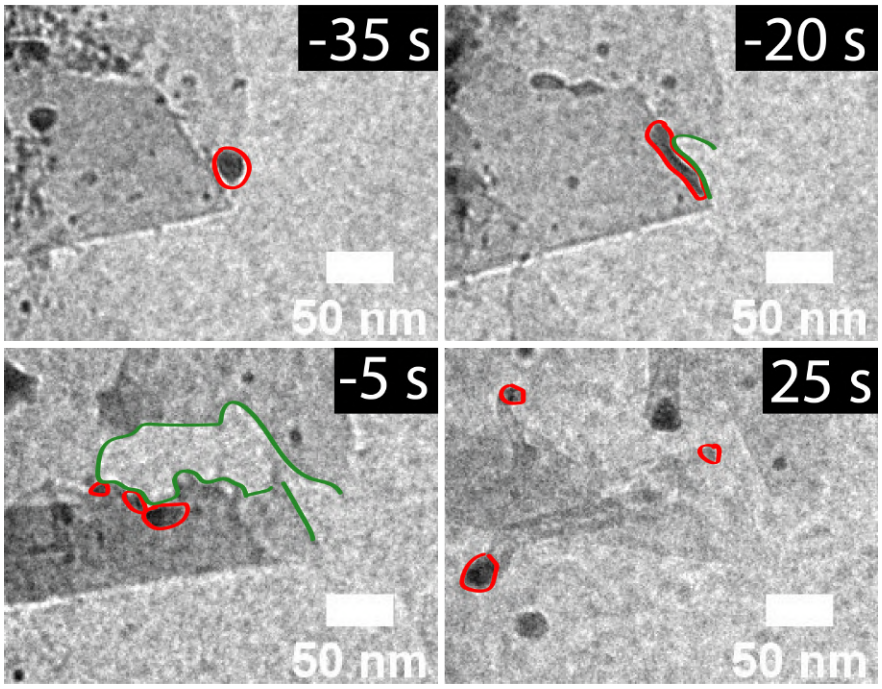

Figure 3.9: In-situ TEM images of Ni/GNP-ox in between switching from reducing atmosphere to reaction atmosphere. The sample holder is under vacuum (4 mbar) until the 3:1 CH_4:H_2 reaction atmosphere is introduced at $t = 0$ s. The temperature is 550 °C. One single Ni particle is highlighted in red. Over time, this particle methanates the carbon support, while splitting up into multiple particles. When the reaction atmosphere is introduced, these particles nucleate CNFs under 550 °C, 1:3 H_2:CH_4, 1 bar, 0.1 sccm at 10 e^- $Å^{-2}$ s^{-1}. Video can be seen in Figure S5.19.

the origin of this effect. It is also found that the carbon growth rate does not determine the growth mode it is in, as Ni/TiO_2 shows lower carbon growth rates compared to Ni/GNP-ox (see Figure 3.7).

To visualize the CNF growth behaviour of the different catalysts, the weighted growth rate deviation ($\sigma_{\text{average}}/\mu_{\text{particle}}$) and growth factor ($f_g$) are presented in Figure 3.11. The standard deviation in CNF growth rate (σ_{average}) of individual particles is divided by their average growth rate (μ_{particle}), in order to fairly compare fast and slow-growing particles. The resulting plot (Figure 3.11 A) thus visualises how steadily CNFs are grown during experiments. Importantly, as we cannot measure CNFs in 3D, growth in the z-axis contributes to these growth rate deviations, so these values will be higher compared to the real standard deviation in growth rates. All data points were acquired from the first image series (0-4 min), except for Ni/SiO_2. Due to rapid CNF growth, an insufficient number of data points could be obtained. Therefore, an alternate stack was used for analysis (8-12 min). It is expected that time differences do not have a significant effect on the value of $\sigma_{\text{average}}/\mu_{\text{particle}}$ (Figure S5.9).
When comparing the different catalysts, Ni/SiO_2 and Ni/TiO_2 show lower $\sigma_{\text{average}}/\mu_{\text{particle}}$ compared to Ni/GNP and Ni/GNP-ox. Therefore a more consistent carbon flow through the Ni particle occurs on the oxide supports compared to the carbon supports. Particle sizes do not seem to influence $\sigma_{\text{average}}/\mu_{\text{particle}}$, meaning the surface-to-volume ratio does not significantly influence how steadily CNFs are grown. Hence, the observed differences in $\sigma_{\text{average}}/\mu_{\text{particle}}$ between carbon and oxide supports may be attributed to a difference in carbon diffusion and output. However, the limited number of data points available for larger particles makes it challenging to make precise statements about the effect of particle size.

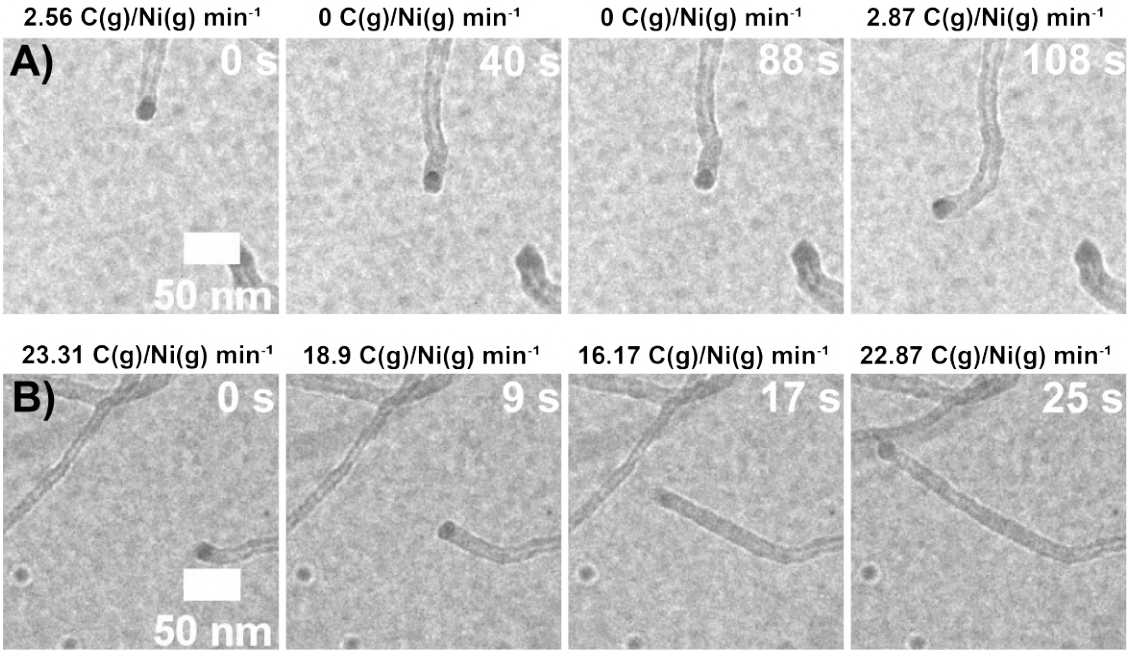

Figure 3.10: In-situ TEM images of stuttering (A) and continuous (B) growth. Time is relative to first frame (0 s). (A) Ni particles supported on GNP can stop (40-88 s) during growth before continuing CNF growth (108 s). See video in Figure S5.21 (B) Ni particles on SiO_2 do not stop growth anytime and perform steady growth. See video in Figure S5.20

In order to characterise the intensity of the 'stuttering' growth on the carbon supports, the growth factor (f_g) is introduced in Figure 3.11 B-C. f_g is defined as the number of frames an individual particle is growing a CNF, divided by the total number of frames that image series, see (2.17). This means that at $f_g = 1$ the fiber is growing nonstop and $f_g = 0.5$ the fiber is growing half the time. f_g growth is thus a numerical value assigned to the degree of how 'continuous' particles grow. Particles listed in Figure 3.11 B-C consist of particles that stop and continue growing *or* grow for the entire stack. Therefore Ni/SiO_2 and Ni/TiO_2 have a growth factor of $f_g = 1$ as they do not stop and continue growth (Figure 3.11 C). Later image series were measured on these, as earlier series did not provide enough data points due to fast CNF growth.
During Ni/GNP and Ni/GNP-ox experiments, smaller particles are standing still more often as f_g is lower. This indicates that there is not enough methane decomposed in order to keep a sustained flow of carbon to the CNF, inhibiting growth. As these should have a relatively larger amount of active sites, these are blocked faster on smaller particles. This is in agreement with smaller particles having a higher surface-to-volume ratio, therefore more carbon deposition and a higher carbon concentration in the particle. This flattens the carbon concentration gradient resulting in slow diffusion and carbon accumulation at the active sites. The balance between carbon input/diffusion/output is better as f_g increases with particle size, meaning these particles grow CNFs more consistently. When the particles reach a diameter of approximately $\geq$ 22 nm (GNP) and $\geq$ 17 nm (GNP-ox), enough carbon is deposited to continuously grow CNFs. It is difficult to compare this growth factor over time, as CNF crowding and catalyst expansion result in a lack of data points in later image series. Still, the f_g of particles on Ni/GNP seems to reduce over time (Figure3.11 B), meaning that active sites are blocked over time. Ni/GNP-ox seems to have a higher f_g at smaller particle sizes. As Ni/GNP-ox showed higher carbon growth rates (Figure 3.7), fewer active sites were blocked. Therefore a more consistent carbon diffusion occur, resulting in steadier growth and a higher f_g.

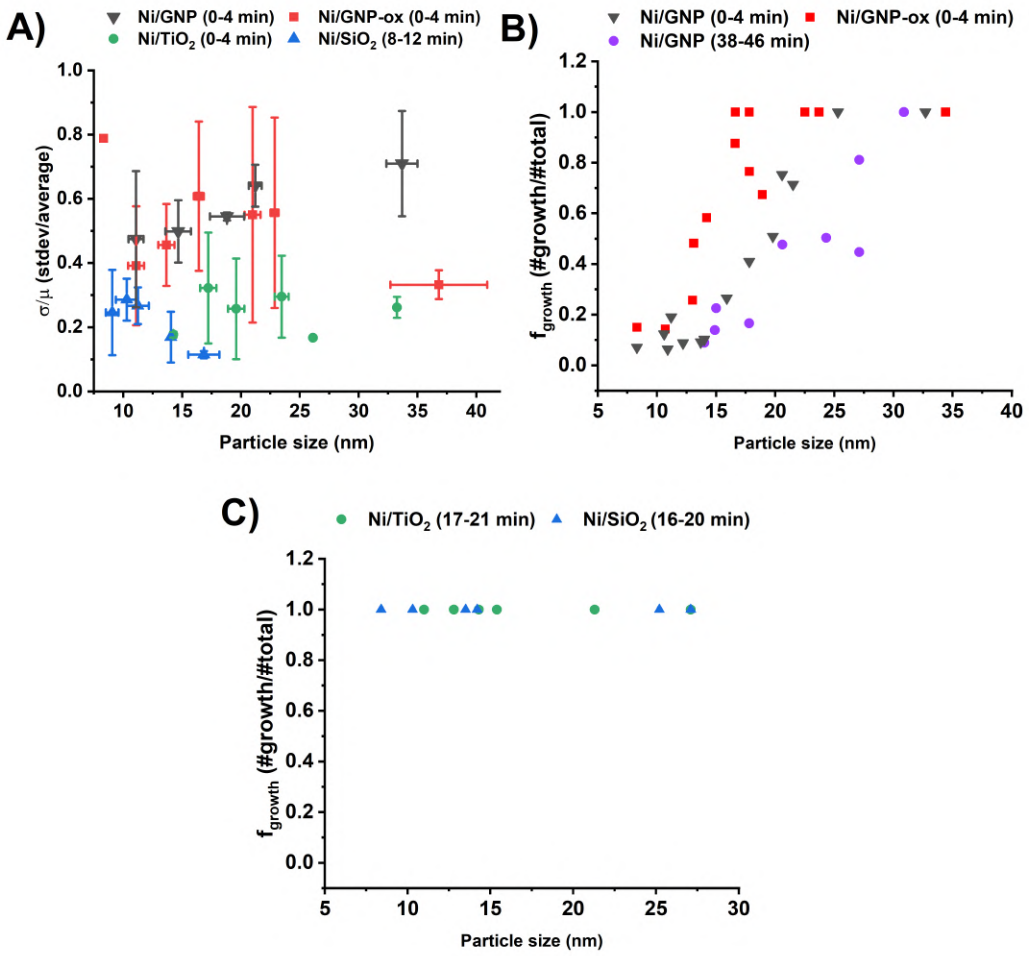

Figure 3.11: A) Average weighted growth rate deviation according to section 2.15. Data points consist of the average carbon growth rate of individual particles, divided by the standard deviation within these growth rates. B) f_g of Ni/GNP and Ni/GNP-ox. C) f_g of Ni/SiO_2 and Ni/TiO_2. Exact conditions for measuring are set in section 2.5.4. Timestamps in the legends refer to the time period of the image series after the start of the experiment.

Interestingly these differences in growth mode, $\sigma_{\text{average}}/\mu_{\text{particle}}$ and f_g are sustained throughout the experiment, even when the Ni particle is lifted from the support and long CNFs are formed. This observation, combined with the difference in the deactivation rate, suggests the support material influences the CNF nucleation phase in such a way different CNF growth dynamics are sustained throughout growth. Several factors may be of importance to these observations. First, during the CNF nucleation phase, carbon is deposited on the support surface between the metal-support interface. The affinity of the support towards carbon may influence the method of deposition on this surface. Second, during CNF nucleation, the particle is elongated before contracting to a more spherical shape during growth (Figure S5.25). This happens because the increase in Ni surface energy cannot be compensated anymore by the binding of graphene to the Ni surface [18]. Differences in metal-support interactions might influence this Ni elongation process by various degrees of compensating for energy losses. And last, differences in surface energy at the metal-support interface result in different contact angles between the particle and the support. Li *et al.* showed that this angle is essential for CNF growth, where in the case of FeCo catalysts an acute angle resulted in base growth

and an obtuse angle in tip growth [22].
These factors contribute to the CNF nucleation phase by interacting with the metal particle differently. And as particles behave liquid-like during experiments, these interactions might enforce a specific particle shape during growth. Therefore different qualities of CNFs can occur, because the herringbone fiber resembles the orientation of the Ni facets during growth. Takenaka *et al.* studied the Raman spectra of CNFs over different support materials and found that the order of graphitisation on Ni/graphite differed from Ni/SiO_2 and Ni/TiO_2 [35]. It was argued that a smaller Ni particle size of 20 nm on graphite versus 26 nm on SiO_2/TiO_2 may have been the cause of this, however, this may also advocate the hypothesis of different particle shapes. Nonetheless, due to low resolutions during in-situ TEM experiments, possible differences in Ni particle shapes during growth are not reliably quantifiable. Ex-situ high-resolution TEM can be used to image carbon deposits on the support and the herringbone CNFs, as differences in the angle of the herringbone fiber should provide information regarding the Ni shape during growth. However, since this will not be discussed in this research, we will need an alternative approach.

In order to still distinguish possible differences in particle shape during growth, individual particles were imaged over a period of time according to section 2.5.5. Multiple images were stacked on top of each other, resulting in an 'average' particle shape. Larger particles were used, as these are constantly in focus and grow slowly enough to clearly judge their growth in the z-axis. Smaller particles would be blurry and difficult to judge regarding their orientation. The result can be seen in Figure 3.12, with the exception of Ni/SiO_2 as no large enough particles fulfilled the set criteria. It can be seen that Ni particles supported on GNP/GNP-ox have a more teardrop-like shape compared to Ni/TiO_2. However, it should be noted that these are single particles of a relatively large size and therefore may not be representative of the total population. Also, small movement in the z-axis is not accounted for, which may quickly alter the observed shape ratios. But as we average out 10 images over a period of time, these deviations are minimised. Particles with sizes between 20-24 nm saw a similar trend regarding a teardrop-shape for carbon supports (Figure S5.10). However, as mentioned particles of these sizes are difficult to characterise reliably.

Teardrop-like shapes have a higher surface-to-volume ratio, providing more carbon deposition to less bulk Ni, raising the Ni_3C concentration in the bulk. And as the carbon concentration gradient is the driving force, this lowers the diffusion, quickly deactivating catalyst particles. This might explain why the deactivation rate on smaller (< 10 nm) particles is intenser on carbon supports compared to oxide supports. Furthermore, teardrop-like shapes might provide more Ni(111) facets to nucleate graphene sheets and introduce shorter diffusion path lengths. Which might explain the slower deactivation rate of larger Ni/GNP-ox and Ni/GNP particles. Overall, these factors provide an imbalance between carbon input/diffusion/output, resulting in different CNF growth dynamics.

The nature of Ni particle shape during growth may thus explain the differences regarding particle size dependency, $\sigma_{\text{average}}/\mu$ and growth mode (expressed as f_{g}) between the carbon and oxide supports. Especially as these differences are sustained throughout the experiment when no direct influence of the support material is possible. Still, future experiments are necessary to conclude if these particle shapes are representative of the total population of the different catalysts.

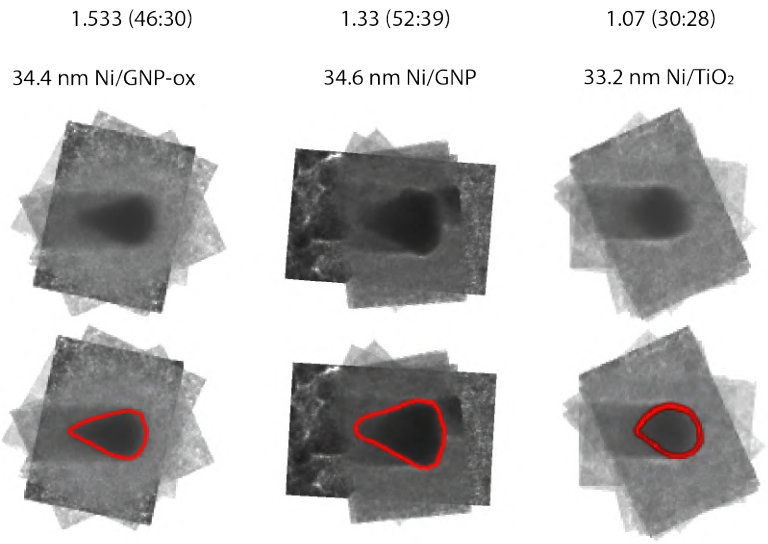

Figure 3.12: Average of projection images of a Ni particle growing a CNF. The same particle was tracked and 10 images were taken every 1 in 5 frames. Images were stacked on top of each other according to section 2.5.5. Length/ height ratios are listed at the top.

3.2.4 H_2-pulse experiments

In-situ TEM experiments were performed to regenerate activity on the partially deactivated Ni/GNP catalysts, called 'H_2-pulse' experiments, see Figure S5.24 and Figure S5.23. The catalysts were exposed to 10% H_2 in Ar for a brief period of time ($\sim$ 30 s) at 550 °C. This would hypothetically remove some encapsulated carbon, reactivating metal surface sites [27]. Like with the Ni/GNP-ox experiments, during the period between switching atmospheres when the gas-cell was under vacuum, severe carbon consumption occurred. Especially the newly grown CNFs were severely consumed, as these consist of relatively many carbon defects [35]. Therefore, these H_2-pulse experiments are divided into two parts. One type of experiment where the reaction atmosphere was introduced via the conventional way, with the intermediate period of vacuum (H_2-Vac). And one type of experiment in which the holder was closed physically when switching reaction atmospheres (H_2-noVac). This way the pressure was maintained around the catalysts. No carbon was visibly consumed during the H_2-pulse itself at 1 bar, emphasising methanation is preferred at low pressures. Significant carbon consumption occurred during the H_2-Vac experiments, as many of the fibers were lost. No visible carbon consumption occurred during the H_2-noVac experiment.

In Figure 3.13, panels A-C present the relevant H_2-Vac data, while panels D-F showcase the H_2-noVac experiment. As seen in Figure 3.13 A and E, the severe carbon consumption during H_2-Vac clearly influences the carbon growth rate, as the activity is increased 3-4 fold, whereas H_2-noVac showed no increase in activity. The severe carbon consumption due to the low pressure in the H_2-Vac experiment thus likely removed more accumulated carbon from the active sites compared to H_2-noVac. In Figure 3.13 B and E, a semi-quantitive overview of the number of Ni particles that were showing any amount of CNF growth is presented. This includes particles that are deactivated during the image series. Despite showing no increase in CNF growth rate, the H_2-pulse increased the number of active particles during the H_2-noVac experiment, as does H_2-Vac. The H_2-pulse procedure thus clearly (re)activated Ni particles during both experiments. In Figure 3.13 C and F, the respective f_g are listed. After both H_2-pulses, the particles show higher f_g, meaning a more consistent growth. Interestingly, the size dependency of this f_g differs between H_2-vac and H_2-noVac. Smaller particles grow more consistently after H_2-noVac compared to H_2-Vac. It is difficult to assign the origin of this observation. One of the possible explanations might be that a higher observed carbon growth

rate after H_2-Vac resulted in smaller particles deactivating quickly, as larger amounts of methane is decomposed, increasing the chance in carbon accumulation at the active sites. Also during H_2-noVac the reaction atmosphere is introduced more steadily as the pressure around the catalyst was maintained at 1 bar. The influence of this slower introduction is still unknown as particles would exhibit less of a 'shock factor' due to the more gradual exposure of methane. Another hypothesis regarding higher f_g might be along the line of different growth shapes. Ni particles interacted differently with the CNFs during H_2-Vac and H_2-noVac. As a result, particles might exhibit a different shape upon continuing growth, which influences the balance between carbon input, diffusion and output. H_2-noVac might thus enforce a better carbon balance.

Nevertheless, the H_2-pulse experiments clearly improved the performance of the Ni/GNP catalysts. It is possible that the H_2-pulse reduced some remaining NiO species, resulting in these particles becoming active. However, this effect is expected to be minimal as 3:1 CH_4:H_2 is a reducing atmosphere. Still, control experiments are needed in order to check if accumulated carbon is actually removed from deactivated sites by H_2.

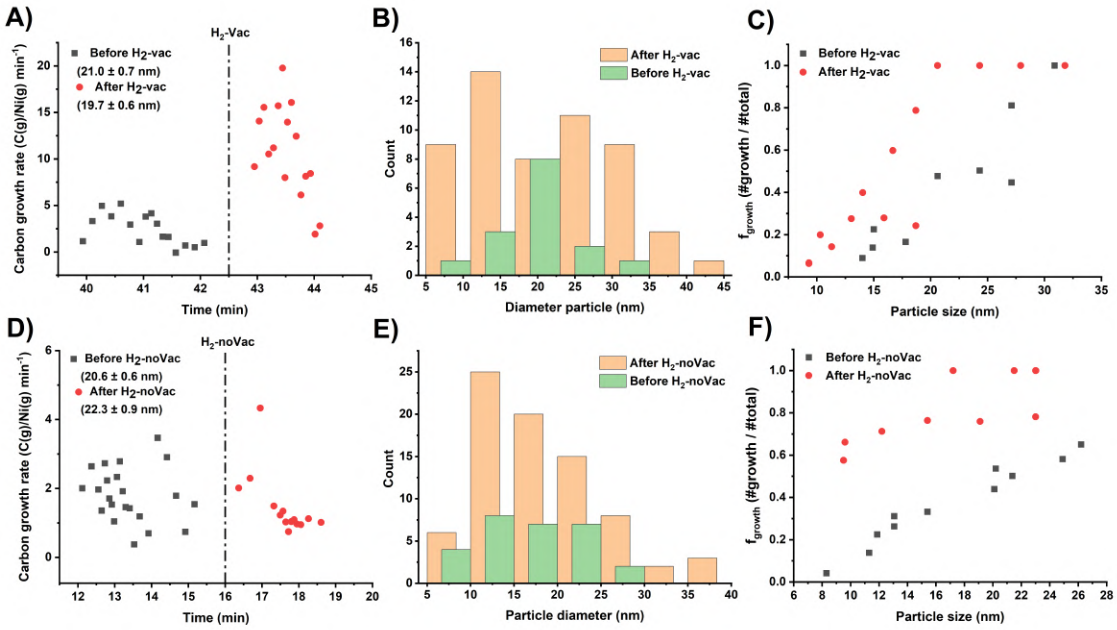

Figure 3.13: H_2-pulse experiments. Deactivating catalysts were exposed to 10% H_2 in Ar for 30 seconds at 550 °C before reintroducing the reaction atmosphere. (550 °C, 1:3 H_2:CH_4, 1 bar, 0.1 sccm at 10 e^- $Å^{-2}$ s^{-1}). A-C represent the H_2-Vac and D-F the H_2-noVac experiments. A, D) Carbon growth rates of multiple particles over time. Growth rates are averaged every 3 data points. B, E) Semi-quantitive analysis of active Ni particles. Particles were only counted when they showed growth outside the support in order to keep a fair comparison. C, F) Growth factor f_g of individual Ni particles.

Chapter 4

Conclusion

In this study, we performed experiments on methane decomposition over synthesised Ni catalysts supported on SiO_2 (aerosil 380), TiO_2 (P90), and pristine/oxidised carbon (GNP-500) using in-situ TEM. Catalysts were synthesised using incipient wetness impregnation (IWI) resulting in well-dispersed Ni nanoparticles over the support surface. Similar-sized particles were grown on all different supports by altering the synthesis procedure. A double impregnation approach was used for Ni/GNP and Ni/GNP-ox and heat treatment programs were adjusted for Ni/SiO_2 and Ni/TiO_2 to achieve this. The IWI synthesis approach for Ni/MgO resulted in the absence of sufficient particles on the support material, likely due to Ni^{2+} migration into the support material. Therefore it was chosen to exclude this catalyst from in-situ TEM experiments.

In-situ TEM experiments saw CNF formation at 550 °C under 75/25% CH_4/H_2. We provided an approach to analysing CNF growth in terms of carbon growth rate. As 3D assumptions were made from 2D electron microscope image projections, this introduced multiple unavoidable inaccuracies. We argued the cause of these and how this is represented in the obtained in-situ TEM data. Carbon growth rates were determined by measuring the amount of carbon grown from a Ni particle over a period of time. As this was done for dozens of various-sized Ni particles per catalyst over a period of 20-50 minutes, similar-sized particles were represented by the average carbon growth rate as a function of time. Smaller particles had higher initial carbon growth rates, which was assigned to an increase in surface-to-volume ratio compared to larger particles. All catalyst particles showed deactivation over time, which was assumed to be due to carbon accumulation at active surface sites [5]. We made several noteworthy observations with respect to particle size:

1. Ni/SiO_2 and Ni/TiO_2 saw no significant particle size effect regarding activity and deactivation.
2. Ni/GNP-ox and Ni/GNP showed significant particle size dependency. Smaller particles (< 10 nm) underwent rapid deactivation within minutes. Upon increasing size, it seemed that deactivation was less severe, however, conclusions are difficult to make because of the large deviations in the carbon growth rate.

It is difficult to state optimal particle sizes as the size ranges of this study were not broad enough. Nevertheless, optimal particle sizes of Ni-based catalysts are dependent on the type of support material and should be investigated separately.

During in-situ TEM experiments, we observed differences in the manner in which CNFs were grown on different supports. Ni on the metal oxide supports had a more 'continuous' growth in which there was little deviation in carbon growth rate, whereas Ni on the carbon supports showed 'stuttering' growth. This was characterized by particles stopping and resuming growth with relatively large growth rate deviations. Numerical values were assigned to these observations in terms of weighted standard deviation ($\sigma_{\text{growth}}/\mu_{\text{size}}$) in

the growth rate and growth factor (f_g). Regarding the support effect on the CNF formation, this led to the following observations:

1. Initial carbon growth rate differed between supports in the order of: Ni/SiO_2 >> Ni/GNP-ox ≈ Ni/TiO_2> Ni/GNP. A stronger interaction of Ni on TiO_2 compared to SiO_2 resulted in the former having slower carbon diffusion, therefore more carbon accumulated on the active sites during the CNF nucleation phase, reducing carbon growth rates.

2. Ni/GNP-ox underwent severe consumption due to support methanation at low pressures prior to catalytic experiments. It is still unknown how significant this effect is. Nevertheless, the activity was superior to Ni/GNP, which is likely a result of support defects promoting CNF formation.

3. Supports influence the manner of carbon growth (continuous vs stuttering) which is hypothetically a consequence of a different particle shape induced by the support during the CNF nucleation phase.

Additional 'H_2-Pulse' experiments regarding the regeneration of deactivating Ni/GNP catalysts were performed. This was done by exposing them to 10% H_2 in Ar for a brief period of time (30 sec), hypothetically removing encapsulated carbon. Experiments in which CNFs were consumed during the period in which the gas-cell was under low pressure significantly increased carbon growth rates. In experiments in which the low pressure atmosphere was avoided, and hence CNF consumption, this effect was less distinct. Both experiments also increased the amount of active Ni particles. More trial experiments are needed to test the effect of an H_2-pulse, nevertheless, it proves to be a promising method of prolonging CNF growth.

On an ending note, in-situ TEM provides us with a unique opportunity to investigate the behaviour of catalytic particles during methane decomposition. While still some trial experiments are needed to verify observations made during this thesis, it provides us with a greater understanding of particle size and support effects during methane decomposition.

4.1 Outlook

As the concluding part of this thesis, this outlook section will discuss what experiments were not performed due to time and practical constraints but are deemed necessary or interesting for increasing our understanding of this topic. Firstly, complementary thermal gravimetric analysis (TGA) can be used to do catalytic experiments as the total weight gain due to formed CNFs is measured. This can validate if the activity and deactivation of individual nanoparticles during in-situ TEM experiments translate to the bulk catalyst performance. As we now characterised the carbon growth rates of individual particles, comparing this to the performance of the bulk catalyst may provide information regarding the number of inactive particles during experiments.

In order to check whether different supports indeed result in a different Ni particle shape during CNF growth, short ($\sim$ 5 min) catalytic TGA experiments should be performed. This will result in relatively short fibers which allow for the CNF-support interface to be imaged using high-resolution TEM (HRTEM). The structure of the deposited carbon at this interface may give clues regarding the CNF nucleation phase. As the structure of the CNFs resembles the shape of the metal particle during growth, HRTEM images can also potentially differentiate particle shapes during growth by measuring the relative angle of graphene sheets in the herringbone fiber.

The performed in-situ TEM experiments have provided us with interesting data. However, it is still undisclosed what the influence of several factors is on the results. To verify results, some control experiments are necessary:

1. As Ni/GNP-ox showed severe support consumption significantly altering support composition, experiments have to be performed without the intermediate vacuum thus avoiding support consumption. As seen in the H_2-pulse experiments, this carbon consumption can significantly influence results.

2. Catalysts were reduced at temperatures determined by TPR. This resulted in Ni/GNP and Ni/GNP-ox being reduced at 350 °C, Ni/SiO_2 at 450 °C and Ni/TiO_2 at 550 °C. Possibly, the difference in temperature can influence the extent to which the particles are reduced, which affects carbon deposition, diffusion and CNF growth. The first indications are that this did not seem the case in our experiments, see Figure S5.8. However, this plot is based on two particles per catalyst and is thus statistically irrelevant. Therefore a control experiment is needed to exclude any effect a higher reduction temperature might have on the activity.

3. Ni/SiO_2 had superior activity compared to the other catalysts. There is a chance that slightly higher electron doses during experiments and the mentioned first come first serve scenario may have contributed to a misleadingly high carbon growth rate. Therefore it may be necessary to repeat this experiment to test the validity of the results. Also for a better comparison of Ni/SiO_2 deactivation over time, longer experiments are needed.

4. During the H_2-pulse experiments, we hypothesised that brief exposure of H_2 to the catalyst removed carbon from the deactivated metal sites, increasing the activity. In order to validate this, the same procedure has to be performed without 10% H_2 in the pulse. If the activity does not change, one is assured that encapsulated carbon is removed and the increase in activity is not an artifact of changing atmospheres.

As Ni/MgO is still a promising catalyst, future efforts should focus on optimising this catalyst for experimental purposes. In this thesis, a beginning was made but Ni particles seemed finely dispersed over the support. Varying heat treatment and reduction programs should be tried first, as these can greatly influence crystallite sizes. An alternative approach might be the use of different precursors. Exchanging the H_2O ligands in nickel nitrate complexes with ethylenediamine [71]. This will raise the pH and remove water in order to avoid dissolving MgO and Mg(OH_2) formation. However, these alternative ligands in non-aqueous solutions

are often significantly less soluble than nickel nitrate. This results in low concentrations and thus low Ni weight loadings using the conventional IWI approach, which is unwanted during in-situ TEM experiments as fewer particles are observed. Therefore, alternative precursors need a different impregnation approach, such as the constant addition of precursor under vacuum drying.

Raman spectroscopy can provide information regarding the CNF quality in terms of D (1380 cm^{-1}, structural imperfections) and G band (1590 cm^{-1}, C-C stretching) of graphitic carbon [35]. The relative intensities of these peaks can be used to determine the quality of grown CNFs on different supports. X-ray photoelectron spectroscopy (XPS) can be used to determine the relative strength of metal-support interactions (MSI) among different supports. This analysis can support the hypothesis that stronger MSI inhibits the lifting of Ni particles, resulting in faster carbon accumulation at the active sites[31]. However specialised equipment is necessary to prevent oxidation of the Ni species at the metal-support interface.

4.2 Acknowledgments

I would like to thank various people for their help and contribution to this project; First Dr. Tom Welling as my daily supervisor, for guidance and helping to conceptualise this research. Also for performing the in-situ TEM experiments and allowing me to present this work at Netherlands' Catalysis and Chemistry Conference (NCCC). Even when he was working in Japan, his extensive interest and feedback were greatly appreciated. Second, Dr. George Tierney for succeeding Tom as daily supervisor, his feedback and suggestions were meaningful for me and the outcome of this project. Furthermore, I want to thank Hans Meeldijk for training me on the Tecnai20 and performing in-situ TEM experiments. The time he made and his interest in this project has been very much appreciated.

I would like to express my gratitude to my first and second supervisors Prof. Dr. Petra de Jongh and Dr. Jessi van der Hoeven for their discussions and useful critiques of this research work. Importantly, I also want to thank Suzan Schoemaker and Kristiaan Helfferich for physisorption measurements and their practical advice regarding catalyst synthesis, Juliette Verschoor for helping me oxidise GNP and for advice regarding these carbon materials, Hidde Nolten for training me on the titration setup, Remco Dalebout for giving advice and instructions on TPR measurements, Dennie Wezendonk for the XRD instructions, and the TEM meeting group for useful discussions during my presentations.

Last but not least, I want to thank my fellow master's students and the whole of MCC for the warm atmosphere and for involving everyone in various activities. I am sure this helped me to be greatly motivated throughout this thesis.

Bibliography

(1) Sánchez-Bastardo, N.; Schlögl, R.; Ruland, H. *Industrial and Engineering Chemistry Research* **2021**, *60*, 11855–11881.

(2) Hybrit direct iron reduction hydrogen, `https://www.hybritdevelopment.se/en/research-project-1/`, Accessed: 2023-06-22.

(3) Agency, I. E. *Global Hydrogen Review 2022*; 2022.

(4) Barelli, L.; Bidini, G.; Gallorini, F.; Servili, S. *Energy* **2008**, *33*, 554–570.

(5) Jong, K. P. D.; Geus, J. W. *Catalysis Reviews - Science and Engineering* **2000**, *42*, 481–510.

(6) Smit, E. D.; Swart, I.; Creemer, J. F.; Hoveling, G. H.; Gilles, M. K.; Tyliszczak, T.; Kooyman, P. J.; Zandbergen, H. W.; Morin, C.; Weckhuysen, B. M.; Groot, F. M. D. *Nature* **2008**, *456*, 222–225.

(7) Wal, R. L. V.; Ticich, T. M.; Curtis, V. E. *Carbon* **2001**, *39*, 2277–2289.

(8) Calvillo, L.; Gangeri, M.; Perathoner, S.; Centi, G.; Moliner, R.; Lázaro, M. J. *Journal of Power Sources* **2009**, *192*, 144–150.

(9) Andersen, S. M.; Borghei, M.; Lund, P.; Elina, Y. R.; Pasanen, A.; Kauppinen, E.; Ruiz, V.; Kauranen, P.; Skou, E. M. *Solid State Ionics* **2013**, *231*, 94–101.

(10) Blackman, J. M.; Patrick, J. W.; Arenillas, A.; Shi, W.; Snape, C. E. *Carbon* **2006**, *44*, 1376–1385.

(11) Wu, H. C.; Li, Y. Y.; Sakoda, A. *International Journal of Hydrogen Energy* **2010**, *35*, 4123–4130.

(12) Zhu, Y.; Yue, H.; Aslam, M. J.; Bai, Y.; Zhu, Z.; Wei, F. *Nanomaterials* **2022**, *12*, DOI: `10.3390/nano12193478`.

(13) Sánchez-Bastardo, N.; Schlögl, R.; Ruland, H. *Chemie-Ingenieur-Technik* **2020**, *92*, 1596–1609.

(14) Li, J.; Croiset, E.; Ricardez-Sandoval, L. *Journal of Molecular Catalysis A: Chemical* **2012**, *365*, 103–114.

(15) Alstrup, I.; Tavarest, M. T. *Journal of catalysis* **1992**, *135*, 147–155.

(16) Muradov, N.; Smith, F.; T-Raissi, A. *Catalysis Today* **2005**, *102-103*, 225–233.

(17) Snoeck, J.-W.; Froment, G. F.; Fowles, M. *JOURNAL OF CATALYSIS* **1997**, *169*, 250–262.

(18) Helveg, S.; López-Cartes, C.; Sehested, J.; Hansen, P. L.; Clausen, B. S.; Rostrup-Nielsen, J. R.; Abild-Pedersen, F.; Nørskov, J. K. *Nature* **2004**, *427*, 426–429.

(19) Lyu, Y.; Wang, P.; Liu, D.; Zhang, F.; Senftle, T. P.; Zhang, G.; Zhang, Z.; Wang, J.; Liu, W. *Small Methods* **2022**, *6*, DOI: `10.1002/smtd.202200235`.

(20) Chen, D.; Christensen, K. O.; Ochoa-Fernández, E.; Yu, Z.; Tøtdal, B.; Latorre, N.; Monzón, A.; Holmen, A. *Journal of Catalysis* **2005**, *229*, 82–96.

(21) Lamouroux, E.; Serp, P.; Kalck, P. *Catalysis Reviews - Science and Engineering* **2007**, *49*, 341–405.

(22) Wang, Y.; Li, B.; Ho, P. S.; Yao, Z.; Shi, L. *Applied Physics Letters* **2006**, *89*, DOI: `10.1063/1.2382735`.

(23) Li, Y.; Li, D.; Wang, G. *Catalysis Today* **2011**, *162*, 1–48.

(24) neries, B.; Smith, Z. L. F. R.; Editors, J. X. Q. *Production of Hydrogen from Renewable Resources*; 2015.

(25) Schoemaker, S. E.; Welling, T. A.; Wezendonk, D. F.; Reesink, B. H.; van Bavel, A. P.; de Jongh, P. E. *Catalysis Today* **2023**, 114110.

(26) Ashik, U. P.; Daud, W. M. W.; Abbas, H. F. *International Journal of Hydrogen Energy* **2017**, *42*, 938–952.

(27) Nakayama *Journal of the Japan Petroleum Institute* **2005**, *48*, 301–307.

(28) Karimi, S.; Bibak, F.; Meshkani, F.; Rastegarpanah, A.; Deng, J.; Liu, Y.; Dai, H. *International Journal of Hydrogen Energy* **2021**, *46*, 20435–20480.

(29) *Reactivity of Carbon Deposited on Nickel-Copper Alloy Catalysts from the Decomposition of Methane.*

(30) Sterk, E. B.; Nieuwelink, A. E.; Monai, M.; Louwen, J. N.; Vogt, E. T.; Filot, I. A.; Weckhuysen, B. M. *JACS Au* **2022**, *2*, 2714–2730.

(31) Liang, W.; Yan, H.; Chen, C.; Lin, D.; Tan, K.; Feng, X.; Liu, Y.; Chen, X.; Yang, C.; Shan, H. *Catalysts* **2020**, *10*, 1–20.

(32) Baker, R. T. K.; Harris, P. S.; Thomas, R. B.; Waite, R. J.

(33) Takenaka, S.; Kobayashi, S.; Ogihara, H.; Otsuka, K. *Journal of Catalysis* **2003**, *217*, 79–87.

(34) Ermakova, M. A.; Ermakov, D. Y.; Kuvshinov, G. G.; Plyasova, L. M. *Journal of Catalysis* **1999**, *187*, 77–84.

(35) Takenaka, S.; Ogihara, H.; Yamanaka, I.; Otsuka, K. *Decomposition of methane over supported-Ni catalysts: effects of the supports on the catalytic lifetime*; 2001, pp 101–110.

(36) Rastegarpanah, A.; Rezaei, M.; Meshkani, F.; Zhang, K.; Zhao, X.; Pei, W.; Liu, Y.; Deng, J.; Arandiyan, H.; Dai, H. *Applied Surface Science* **2019**, *478*, 581–593.

(37) Li, X.; Zhang, Y.; Smith, K. J. *Applied Catalysis A: General* **2004**, *264*, 81–91.

(38) Visser, N. L.; Verschoor, J. C.; Smulders, L. C.; Mattarozzi, F.; Morgan, D. J.; Meeldijk, J. D.; van der Hoeven, J. E.; Stewart, J. A.; Vandegehuchte, B. D.; de Jongh, P. E. *Catalysis Today* **2023**, *418*, DOI: 10.1016/j.cattod.2023.114071.

(39) Loosdrecht, J. V. D.; Kraan, A. M. V. D.; Dillen, A. J. V.; Geus, J. W. *Journal of catalysis* **1997**, *170*, 217–226.

(40) Naresh, G.; Kumar, V. V.; Anjaneyulu, C.; Tardio, J.; Bhargava, S. K.; Patel, J.; Venugopal, A. *International Journal of Hydrogen Energy* **2016**, *41*, 19855–19862.

(41) Van Deelen, T. W.; Mejía, C. H.; de Jong, K. P. *Nature Catalysis* **2019**, *2*, 955–970.

(42) Williams, D. B.; Carter, C. B., *Transmission Electron Microscopy: Part 1: Basic*, 2nd; Springer: New York, NY, 2019.

(43) Dai, S.; Gao, W.; Zhang, S.; Graham, G. W.; Pan, X. *MRS Communications* **2017**, *7*, 798–812.

(44) Figueiredo, J. L.; Pereira, M. F. R. *Catalysis Today* **2010**, *150*, 2–7.

(45) Shafeeyan, M. S.; Daud, W. M. A. W.; Houshmand, A.; Shamiri, A. *Journal of Analytical and Applied Pyrolysis* **2010**, *89*, 143–151.

(46) Ros, T. G.; Dillen, A. J. V.; Geus, J. W.; Koningsberger, D. C. *Chemistry Europe* **2002**, *8*, 1151–1161.

(47) Zhuravlev, L. T. *Colloids and Surfaces A: Physicochemical and Engineering Aspects* **2000**, *173*.

(48) Primet, M.; Mathieu, M.-v.; by Michel Primet; Pichat, P.; Mathieu, M.-V. *The Journal of Physical Chemistry* **1971**, *75*, 1216–1222.

(49) Hornak, J.; Trnka, P.; Kadlec, P.; Michal, O.; Mentlík, V.; Šutta, P.; Csányi, G. M.; Tamus, Z. Á. *Nanomaterials* **2018**, *8*, DOI: 10.3390/nano8060381.

(50) Wen, X.; Xu, L.; Chen, M.; Shi, Y.; Lv, C.; Cui, Y.; Wu, X.; Cheng, G.; e. Wu, C.; Miao, Z.; Wang, F.; Hu, X. *Applied Catalysis B: Environmental* **2021**, *297*, DOI: 10.1016/j.apcatb.2021.120486.

(51) Tao, M.; Meng, X.; Lv, Y.; Bian, Z.; Xin, Z. *Fuel* **2016**, *165*, 289–297.

(52) De Jong, K. P., *Synthesis of solid catalysts*, 2009, p 401.

(53) Brockner, W.; Ehrhardt, C.; Gjikaj, M. *Thermochimica Acta* **2007**, *456*, 64–68.

(54) Sietsma, J. R.; Meeldijk, J. D.; Breejen, J. P. D.; Versluijs-Helder, M.; Dillen, A. J. V.; Jongh, P. E. D.; Jong, K. P. D. *Angewandte Chemie - International Edition* **2007**, *46*, 4547–4549.

(55) Gates-Rector S.; Blanton, T. *Powder Diffr.* **2019**, *34*, 352–360.

(56) National Institutes of Health ImageJ, https://imagej.nih.gov/ij/, Accessed: June 2, 2022, 2023.

(57) Adobe Inc. Adobe Photoshop, version CS6, 2023.

(58) Spurr, R. A.; Myers, H. *Analytical chemistry* **1997**, 760–761.

(59) Hanaor, D. A.; Sorrell, C. C. *Journal of Materials Science* **2011**, *46*, 855–874.

(60) Ho, S.-W.; Chu, C.-Y.; Chen, S.-G. *Journal of Catalysis* **1998**, *178*, 34–48.

(61) Parmaliana', A.; Arena, F.; Frusteri, F.; Giordano, N. *J. CHEM. SOC. FARADAY TRANS* **1990**, *86*, 2663–2669.

(62) Chen, L.; Sun, X.; Liu, Y.; Li, Y. *Applied Catalysis A: General* **2004**, *265*, 123–128.

(63) Wang, F.; Han, B.; Zhang, L.; Xu, L.; Yu, H.; Shi, W. *Applied Catalysis B: Environmental* **2018**, *235*, 26–35.

(64) Chen, J.; Yao, N.; Wang, R.; Zhang, J. *Chemical Engineering Journal* **2009**, *148*, 164–172.

(65) Bertella, F.; Concepción, P.; Martínez, A. *Catalysis Today* **2017**, *289*, 181–191.

(66) Shah, M.; Mesfer, M. K. A.; Danish, M. *Fuel* **2022**, *330*, DOI: 10.1016/j.fuel.2022.125596.

(67) Zhuang, H. L.; Zheng, G. P.; Soh, A. K. *Computational Materials Science* **2008**, *43*, 823–828.

(68) Rinaldi, A.; Tessonnier, J. P.; Schuster, M. E.; Blume, R.; Girgsdies, F.; Zhang, Q.; Jacob, T.; Abd-Hamid, S. B.; Su, D. S.; Schlögl, R. *Angewandte Chemie - International Edition* **2011**, *50*, 3313–3317.

(69) Zhang, G. Y.; Ma, X. C.; Zhong, D. Y.; Wang, E. G. *Journal of Applied Physics* **2002**, *91*, 9324–9332.

(70) He, C.; Zhao, N.; Shi, C.; Du, X.; Li, J. *Journal of Alloys and Compounds* **2007**, *433*, 79–83.

(71) Espinosa-Alonso, L.; Jong, K. P. D.; Weckhuysen, B. M. *Journal of Physical Chemistry C* **2008**, *112*, 7201–7209.

Chapter 5

Appendix

A1: Catalyst characterisation

Table 5.1: Effect of the weight loading on particle size. Different concentrations of precursor were used to obtain the different catalysts. The same impregnation procedures were used.

Ni weight loading (wt.%)	Ni (M)	Heat treatment	Reduction temperature (°C)	Ni crystal size TEM (nm)
4.6	1.0	350 °C in N_2	450 (N_2)	16.1 ± 4.7
9	2.3	350 °C in N_2	300 (N_2)	20.1 ± 5.1
17.5	4.0	350 °C in N_2	500 (1:20 NO:N_2)	19.2 ± 6.2

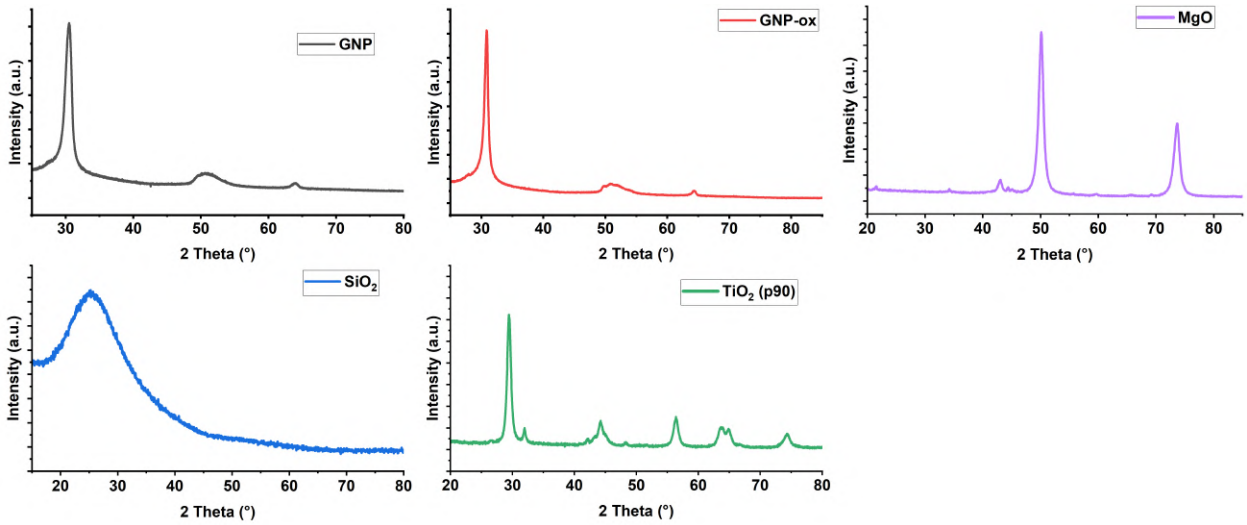

Figure 5.1: Powder X-ray diffraction of unimpregnated support materials.

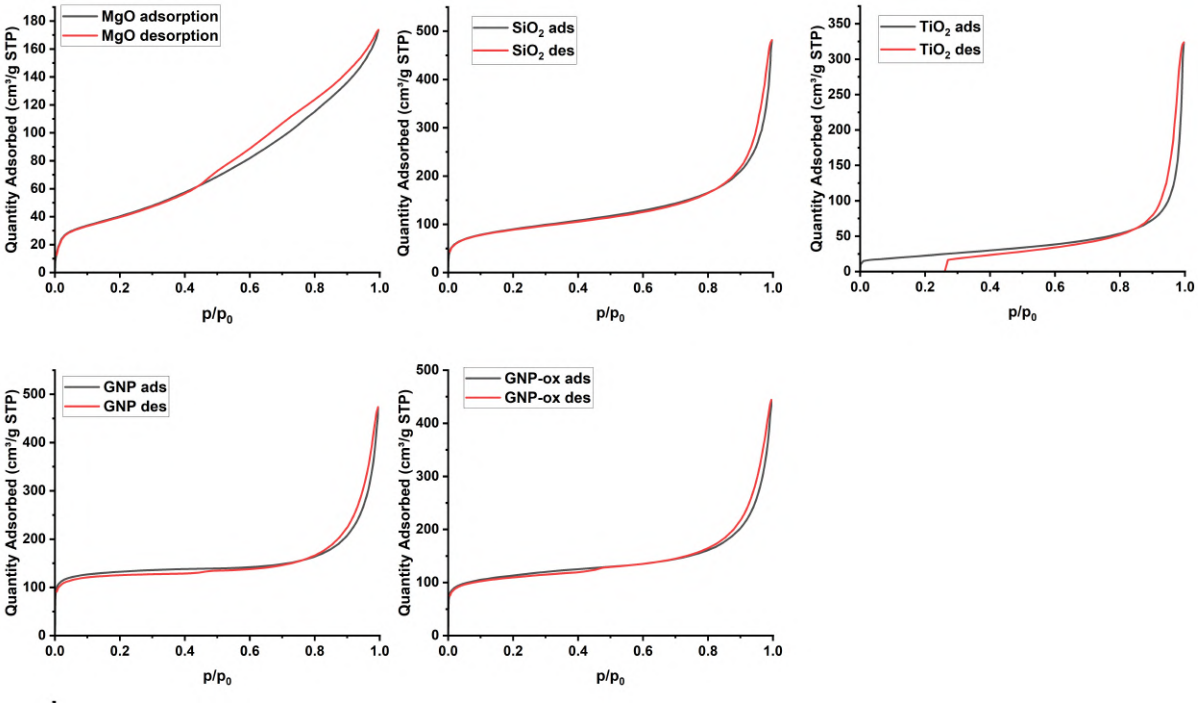

Figure 5.2: N_2-physisorption isotherms of support materials. Adsorption and desorption was measured.

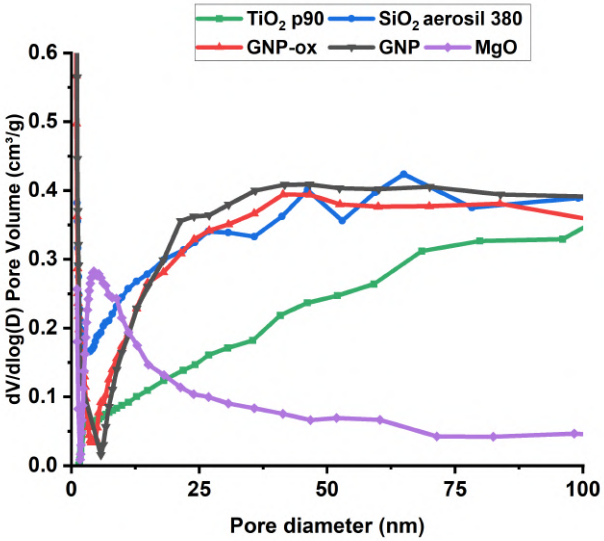

Figure 5.3: Comparison of pore size distribution on bare support materials, obtained from BJH adsorption using the Harkins-Jura t-curve.

Table 5.2: Impregnation details for prepared catalysts. Ni/GNP and Ni/GNP were double-impregnated.

Support	Used pore volume ($cm^3\ g^{-1}$)	Ni (M)	Precursor solvent	Density solution (g cm^{-3})	Mass support (g)	Mass added solution (g)
GNP	0.9	4	H_2O	1.5582	1.2195	1.5396
GNP-ox	0.7	4	H_2O	1.5582	1.7531	1.6442
NiO/GNP	0.3	4	H_2O	1.5582	0.1717	0.1440
NiO/GNP-ox	0.3	4	H_2O	1.5582	0.2498	0.2236
SiO_2	0.8	4	H_2O	1.5582	0.5698	0.6830
TiO_2	0.5	4	H_2O	1.5582	1.1001	0.7469
MgO	0.8	1	EtOH	0.9369	1.9194	1.53984
MgO	0.8	4	H_2O	1.5582	1.6404	1.9203

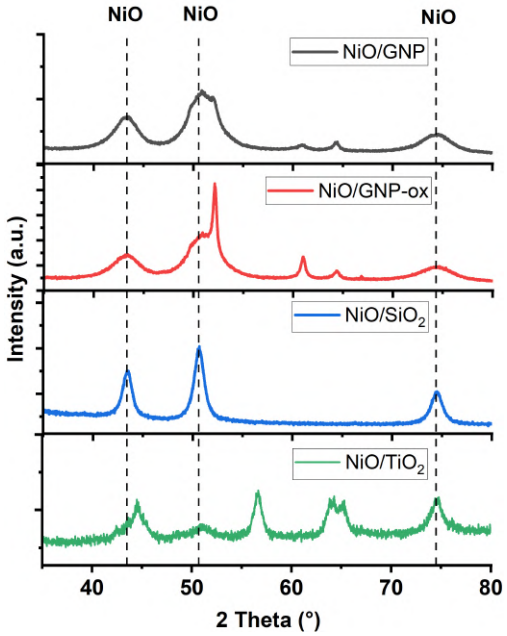

Figure 5.4: Powder X-ray Diffraction of oxidized catalysts samples.

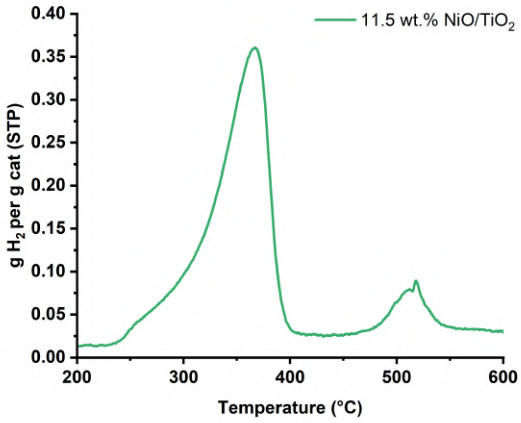

Figure 5.5: Temperature-programmed reduction profile of NiO supported on TiO_2. No oxidation treatment was performed before the measurement. Temperature program: 100-700 °C, 3 °C/min, 5% H_2/Ar (40 mL/min).

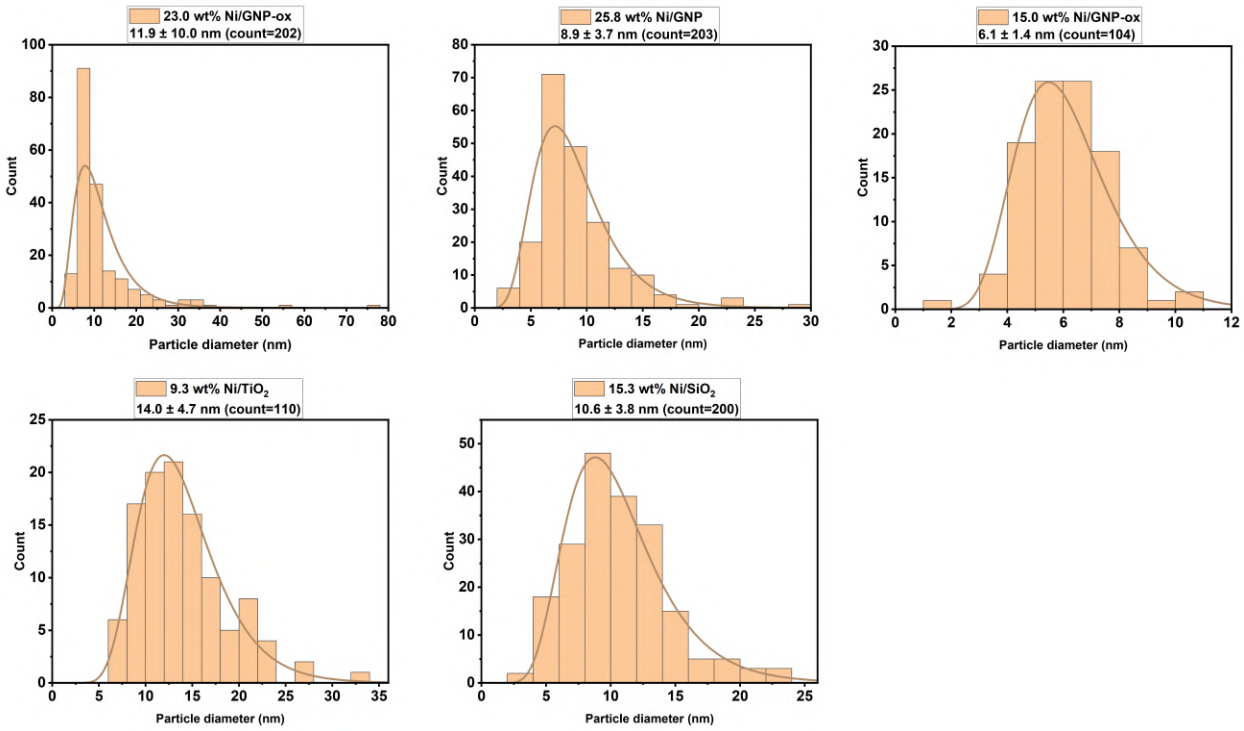

Figure 5.6: Particle diameters determined from TEM images (Tecnai20). Only 110 particles were counted for Ni/TiO_2 due to the low contrast hindering measurements.

A2: In-situ TEM experiments

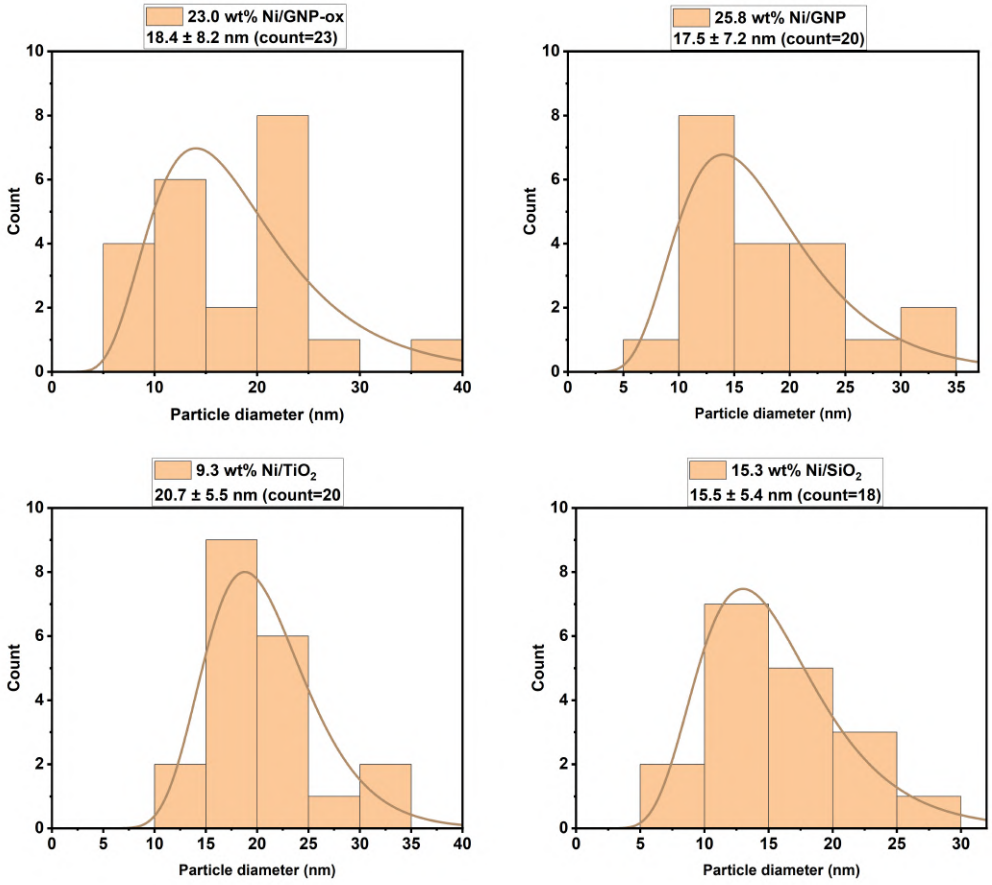

Figure 5.7: Particle size distribution of measured Ni particles analysed from in-situ TEM image series. These particles fulfilled set criteria in section 2.5.1. All experiments were performed at 550 °C, 1:3 H_2:CH_4, 0.1 sccm, 1 bar. Electron intensities during Ni/GNP/GNP-ox/TiO_2 were 10 e^- $Å^{-2}$ s^{-1}, during Ni/SiO_2 was 13 e^- $Å^{-2}$ s^{-1}.

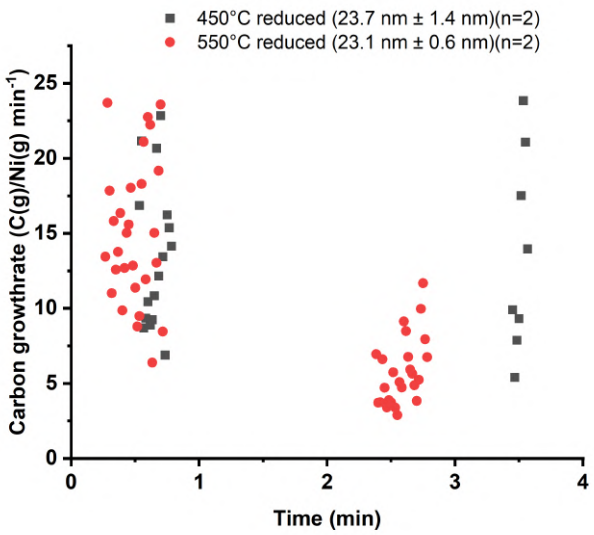

Figure 5.8: Carbon growth rates measured per second, analysed from in-situ TEM image series according to 2.5.1. n is the particle population. All experiments were performed at 550 °C, 1:3 H_2:CH_4, 0.1 sccm, 1 bar. Electron intensities were 10 e^- $Å^{-2}$ s^{-1}.

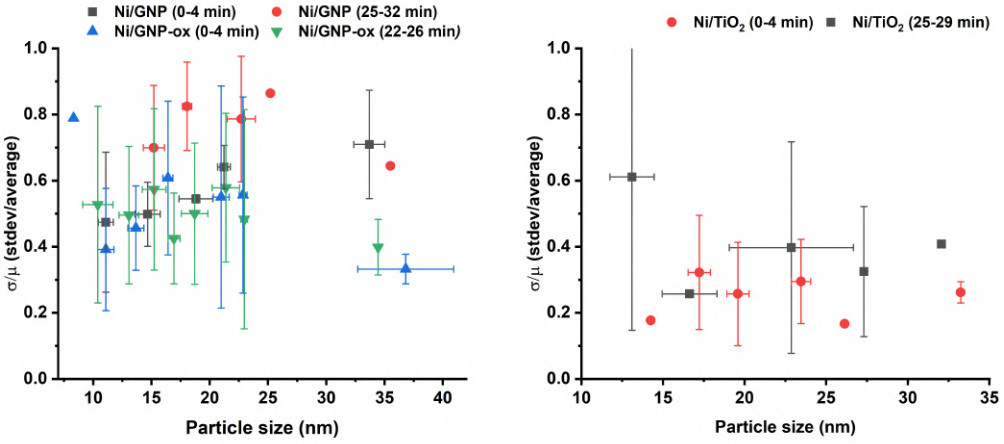

Figure 5.9: Average weighted growth rate deviation according to section 2.15. Data points consist of the average carbon growth rate of individual particles, divided by the standard deviation within these growth rates. Timestamps in the legend refer to the time period of the image series after the start of the experiment.

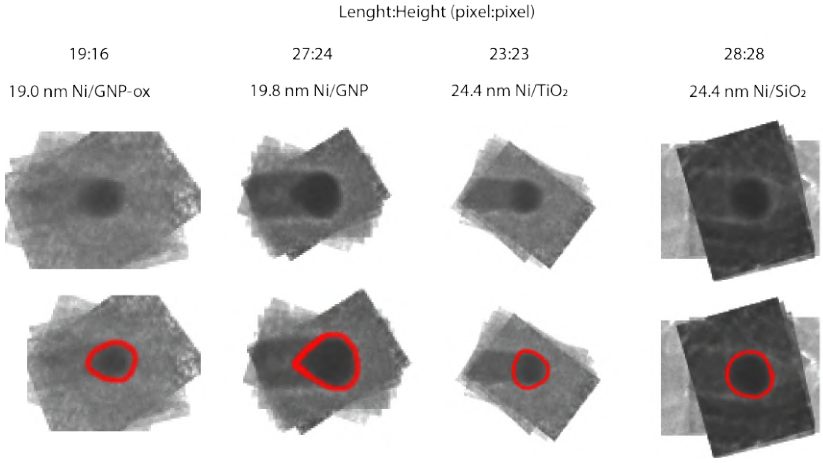

Figure 5.10: Average of projection images of an individual Ni particle growing a CNF. The same particle was tracked and 10 images were taken every 1 in 5 frames. Images were stacked on top of each other according to section 2.5.5. Length: height ratios are listed at the top.

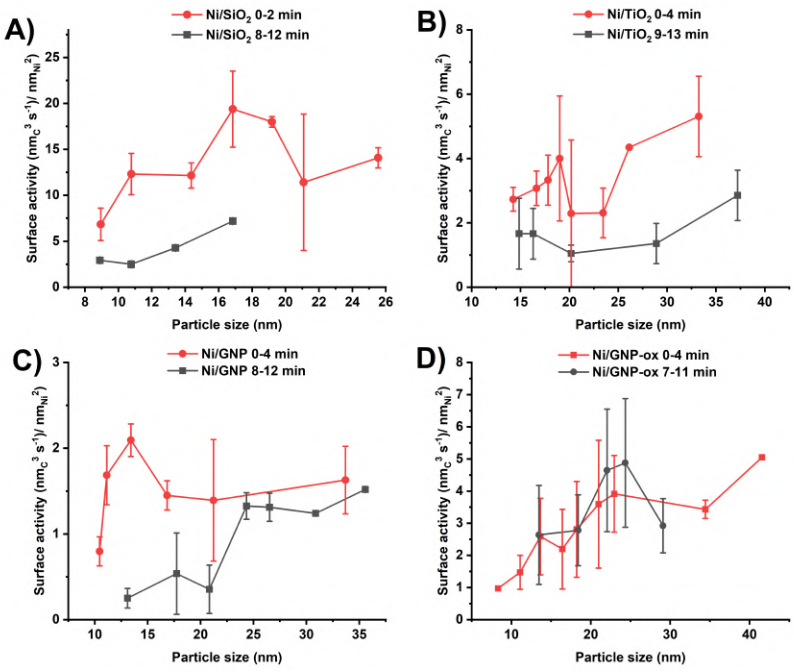

Figure 5.11: Volume of carbon grown per surface area, analysed from in-situ TEM image series according to 2.5.1. All experiments were performed at 550 °C, 1:3 H_2:CH_4, 0.1 sccm, 1 bar. Electron intensities were A) 13 B) 10 C) 10 D) 10 e^- $Å^{-2}$ s^{-1}

Figure 5.12: In-situ TEM experiment of Ni/GNP-ox. The experiment was performed at 550 °C, 1:3 H_2:CH_4, 0.1 sccm, 1 bar. One frame per second. Electron doses of 10 e^- $Å^{-2}$ s^{-1} . Hyperlink: GB023C Ni/GNP-ox.mp4

Figure 5.13: In-situ TEM experiment of Ni/GNP. The experiment was performed at 550 °C, 1:3 H_2:CH_4, 0.1 sccm, 1 bar. One frame per second. Electron doses of 10 e^- $Å^{-2}$ s^{-1}. Hyperlink: GB024C Ni/GNP.mp4

Figure 5.14: In-situ TEM experiment of Ni/TiO_2. The experiment was performed at 550 °C, 1:3 H_2:CH_4, 0.1 sccm, 1 bar. One frame per second. Electron doses of 10 e^- $Å^{-2}$ s^{-1}. Hyperlink: GB018 Ni/TiO_2.mp4

Figure 5.15: In-situ TEM experiment of Ni/SiO_2. The experiment was performed at 550 °C, 1:3 H_2:CH_4, 0.1 sccm, 1 bar. One frame per second. Electron doses of 13 e^- $Å^{-2}$ s^{-1}. Hyperlink: GB010 Ni/SiO_2.mp4

Figure 5.16: Encapsulation of active Ni particle. In-situ TEM experiment of Ni/GNP. The experiment was performed at 550 °C, 1:3 H_2:CH_4, 0.1 sccm, 1 bar. One frame per second. Electron doses of 10 e^- $Å^{-2}$ s^{-1}. Hyperlink: EncapsulationGB024CNi/GNP.mp4

Figure 5.17: Collision of a deactivated Ni particle with an active Ni particle. Particle agglomerates and proceeds to grow. In-situ TEM experiment of Ni/GNP. The experiment was performed at 550 °C, 1:3 H_2:CH_4, 0.1 sccm, 1 bar. One frame per second. Electron doses of 10 e^- $Å^{-2}$ s^{-1}. Hyperlink: Particle CollisionGB024CNi/GNP.mp4

Figure 5.18: Base growth over Ni/TiO_2. The experiment was performed at 550 °C, 1:3 H_2:CH_4, 0.1 sccm, 1 bar. One frame per second. Electron doses of 10 e^- $Å^{-2}$ s^{-1}. Hyperlink: Base growthGB018 Ni/TiO_2.mp4

Figure 5.20: Example of continuous growth during Ni/SiO_2 experiment. The experiment was performed at 550 °C, 1:3 H_2:CH_4, 0.1 sccm, 1 bar. One frame per second. Electron doses of 13 e^- $Å^{-2}$ s^{-1}. Hyperlink: Continuous growth GB010 Ni/SiO_2.mp4

Figure 5.22: CNF eating during vacuum period before H_2-vac experiment on Ni/GNP. The experiment was performed at 550 °C, 1:3 H_2:CH_4, 0.1 sccm, 1 bar. One frame per second. Electron doses of 10 e^- $Å^{-2}$ s^{-1}. Hyperlink: Fiber eaten H_2-vacGB024C Ni/GNP.mp4

Figure 5.19: Support methanation prior to the Ni/GNP-ox experiment. The shift is the moment the gas is introduced. The experiment was performed at 550 °C, 1:3 H_2:CH_4, 0.1 sccm, 1 bar. One frame per second. Electron doses of 10 e^- $Å^{-2}$ s^{-1}. Hyperlink: Support methenationGB023C Ni/GNP-ox.mp4

Figure 5.21: Example of stuttering growth during Ni/GNP experiment. Ni particle proceeds to grow CNF after showing no growth and stops again after a period of time. The experiment was performed at 550 °C, 1:3 H_2:CH_4, 0.1 sccm, 1 bar. One frame per second. Electron doses of 10 e^- $Å^{-2}$ s^{-1}. Hyperlink: Stuttering growthGB024C Ni/GNP.mp4

Figure 5.23: H_2-vac experiment, with the intermediate vacuum period consuming CNFs. Each shift is due to reaction atmosphere introduced, timers are relative to this introduction. The experiment was performed at 550 °C, 1:3 H_2:CH_4, 0.1 sccm, 1 bar. One frame per second. Electron doses of 10 e^- $Å^{-2}$ s^{-1}. Hyperlink: H_2-vacGB024C Ni/GNP.mp4

Figure 5.24: H_2-noVac experiment, with the intermediate vacuum period consuming CNFs. Each shift is due to reaction atmosphere introduced, timers are relative to this introduction. The experiment was performed at 550 °C, 1:3 H_2:CH_4, 0.1 sccm, 1 bar. One frame per second. Electron doses of 10 e^- $Å^{-2}$ s^{-1}. Hyperlink: H_2-noVacGB024C Ni/GNP.mp4

Figure 5.25: In-situ TEM experiment of Ni/GNP-ox. Upon lifting from the support material, the Ni particle is elongated The experiment was performed at 550 °C, 1:3 H_2:CH_4, 0.1 sccm, 1 bar. One frame per second. Electron doses of 10 e^- $Å^{-2}$ s^{-1} . Hyperlink: GB023C Ni/GNP-ox Particle elongation.mp4